THE ASTROPHYSICAL JOURNAL, 435:577–598, 1994 November 10

DEEP *HST*[1] IMAGING OF DISTANT WEAK RADIO AND FIELD GALAXIES

R. A. WINDHORST,[2,3] J. M. GORDON, S. M. PASCARELLE,[2] AND P. C. SCHMIDTKE[2]
Department of Physics and Astronomy, Arizona State University, Box 871504, Tempe, AZ 85287-1504
W. C. KEEL AND J. M. BURKEY
Department of Physics and Astronomy, University of Alabama, P.O. Box 870324, Tuscaloosa, AL 35487
AND
J. S. DUNLOP
Liverpool John Moores University, Chemical & Physical Sciences, Byrom Street, Liverpool, L3 3AF, UK
Received 1993 September 21; accepted 1994 May 10

ABSTRACT

We present deep *Hubble Space Telescope* (*HST*) Wide-Field Camera V- and I-band images of three distant weak radio galaxies with $z = 0.311$–2.390 and seven field galaxies with $z = 0.131$–0.58. The images were deconvolved with both the Lucy and multiresolution CLEAN methods, which yield a restoring FWHM of $\lesssim 0\farcs2$, (nearly) preserve photons *and* signal-to-noise ratio at low spatial frequencies, and produce consistent light profiles down to our 2 σ surface brightness sensitivity limit of $V \sim 27.2$ and $I \sim 25.9$ mag arcsec^{-2}. Multicomponent image modeling was used to provide deconvolution-independent estimates of structural parameters for symmetric galaxies. We present 12-band (m_{2750} *UBVRIgriJHK*) photometry for a subset of the galaxies and bootstrap the unknown FOC/48 zero point at 2750 Å in three independent ways (yielding $m_{2750} = 21.34 \pm 0.09$ mag for 1.0 e^- s^{-1}).

Two radio galaxies with $z = 0.311$ and 0.528, as well as one field galaxy with $z = 0.58$, have the colors and spectra of early-type galaxies, and $a^{1/4}$-like light profiles in the *HST* images. The two at $z > 0.5$ have little or no color gradients in $V-I$ and are likely giant ellipticals, while the $z = 0.311$ radio galaxy has a dim exponential disk and is likely an S0. Six of the seven field galaxies have light profiles that indicate (small) inner bulges following $a^{1/4}$ laws and outer exponential disks, both with little or no color gradients. These are (early-type) spiral galaxies with $z = 0.131$–0.528. About half have faint companions or bars. One shows lumpy structure, possibly a merger.

The compact narrow-line galaxy 53W002 at $z = 2.390$ has $\lesssim 30\% \pm 10\%$ of its *HST* V and I flux in the central kiloparsec (due to its weak AGN). Most of its light ($V \simeq 23.3$) occurs in a symmetric envelope with a regular $a^{1/4}$-like profile of effective radius $a \simeq 1\farcs1$ ($\simeq 12$ kpc for $H_0 = 50$, $q_0 = 0.1$). Its (*HST*) $V-I$ color varies at most from ~ 0.3 mag at $a \simeq 0\farcs2$ to ~ 1.2 mag at $a \gtrsim 0\farcs4$, and possibly to $\gtrsim 2.2$ mag at $a \gtrsim 1\farcs2$. Together with its $I-K$ color ($\simeq 2.5$ mag for $a \gtrsim 1\farcs0$–$2\farcs0$), this is consistent with an aging stellar population ~ 0.3–0.5 Gyr old in the galaxy center ($a \lesssim 2$ kpc radius), and possibly ~ 0.5–1.0 Gyr old at $a \gtrsim 10$ kpc radius. While its outer part may thus have started to collapse at $z = 2.5$–4, its inner part still is aligned with its redshifted Lyα cloud and its radio axis, possibly caused by star formation associated with the radio jet, or by reflection from its AGN cone.

Subject headings: galaxies: evolution — galaxies: photometry — galaxies: stellar content — galaxies: structure

1. INTRODUCTION

To understand the cosmological evolution of weak radio sources and the spectral evolution of their parent galaxies, we must first determine their nature at intermediate to large redshifts (Kron, Koo, & Windhorst 1985, hereafter KKW; Windhorst et al. 1985; 1991, hereafter W91; 1993b, hereafter W93b). Ground-based spectroscopy allows redshift determination and crude spectral classification of powerful radio sources up to $z \lesssim 4$ (e.g., Chambers, Miley, & van Breugel 1990) and of weak radio sources up to $z \sim 2.5$ (Windhorst, Mathis, & Neuschaefer 1990, hereafter W90; W91). However, *morphological* classification is only possible from ground-based images out to $z \lesssim 0.1$–0.2% and is always limited by atmospheric conditions on even the best sites. Also, the surface brightness (SB) sensitivity required to image high-redshift galaxies is fundamentally limited by the bright ground-based night sky, especially in the far-red (and by the bolometric $(1+z)^4$ cosmological SB dimming).

A very important step in the study of the nature and evolution of weak radio galaxies is therefore a systematic study of their optical sub-kiloparsec morphology at redshifts $z \gtrsim 0.3$, where the cosmological evolution of weak radio sources takes off rather rapidly (W90). This can be done through deep imaging with the *Hubble Space Telescope* (*HST*) Wide-Field Camera (WFC), even with *HST*'s aberrated primary mirror, since (1) *HST*'s point-spread function (PSF) has a much narrower core (FWHM $\lesssim 0\farcs1$) than can be achieved from the ground, (2) its PSF is much more stable than is possible from the ground (so that deconvolution with appropriate PSF stars can be done), and (3) the I-band sky background in space is 2–3 mag darker than from the ground (Windhorst, Mathis, & Keel 1992, hereafter W92).

[1] Based on observations with the NASA/ESA *Hubble Space Telescope*, obtained at the Space Telescope Science Institute, which is operated by the Association of Universities for Research in Astronomy, Inc., under NASA contract NAS5-26555.

[2] Optical observations obtained in part at the Multiple Mirror Telescope Observatory, a joint facility of the University of Arizona and the Smithsonian Institution.

[3] Alfred P. Sloan Research Fellow.

In this paper, we present the main results of a Cycle 1 *HST* project to image weak radio galaxies. In earlier papers, we showed that *HST* WFC images can be deconvolved to (a Nyquist-limited) resolution $\lesssim 0\farcs2$ FWHM while largely preserving photons (see §§ 2.4 and 3 here; King et al. 1991, hereafter K91; Keel 1991; W92; Windhorst et al. 1994c, hereafter W94c). Our *HST* images were designed to study (1) the optical morphology and light profiles of high-SB weak radio galaxies out to large redshifts, (2) close companions, merger remnants, and other dynamical disturbances at kiloparsec scales, (3) color gradients to constrain their stellar populations at kiloparsec scales, and (4) their morphology compared to *optically* selected high-redshift early-type galaxies, and to the ultraluminous and morphologically peculiar high-redshift radio galaxies.

At millijansky levels, the weak radio source population is sampled extensively by the Leiden-Berkeley Deep Survey (LBDS; Windhorst, van Heerde, & Katgert 1984b, hereafter WHK; Windhorst, Kron, & Koo 1984a; hereafter WKK). These are dominated by red, high-SB galaxies with colors and spectra of passively evolving giant ellipticals (gEs) with current ages of 10–15 Gyr (KKW; Windhorst, Koo, & Spinrad 1986). We decided to observe *weak* radio galaxies, because their optical properties are generally not dominated by an AGN, yielding a selection of high-redshift galaxies that may give us a good view of their stellar population. The current sample forms a pilot study of radio galaxies with $z = 0.311$–2.390 and field galaxies with $z = 0.131$–0.58 to demonstrate the feasibility of the project, even with the aberrated *HST* optics. Two of the weak LBDS radio galaxies are at moderate redshifts and have (barely) resolved ground-based images on deep Mayall 4 m plates: 53W044 with $V = 19.4$ at $z = 0.311$ and 53W046 with $V = 21.1$ at $z = 0.528$ (WKK).

We also present Faint Object Camera (FOC)/48 images in the F275W filter on these objects to constrain their UV flux. This is being followed up by a Cycle 2 Faint Object Spectrograph (FOS) project of UV spectroscopy for the same and other weak radio galaxies, to trace the evolution of the UV upturn in early-type galaxies with cosmic time (Windhorst et al. 1994b; Pascarelle et al. 1994). We also present further analysis of the very deep *HST* images of 53W002, the highest redshift radio galaxy thus far found in the LBDS (W91). This radio source was identified with a young compact galaxy ($V_{\rm tot} \sim 22.9$) with narrow emission lines at $z = 2.390$ and age of its dominant starburst ~ 0.3 Gyr. It is surrounded by several other possibly Lyα-emitting objects, perhaps a group or cluster of forming galaxies. Our best ground-based continuum images show marginal alignment with the radio source axis, which itself is aligned with the much larger Lyα cloud (W91) Jet-induced star formation or nonthermal radiation scattered in a cone are the most commonly invoked radiation processes in the ultraluminous high-redshift 3CR and 1 Jy radio galaxies (Chambers et al. 1990; McCarthy, Kapahi, & van Breugel 1990; Miley et al. 1992). It is not clear whether these processes are universal or represent some property of the ultraluminous high-redshift radio galaxies (i.e., redshift or radio power), so this needs to be checked with ~ 100 times weaker radio galaxies like those in the LBDS. An overview of the WFC images on 53W002 has been given by W92.

Our deep *HST* images also offer an opportunity to study faint field galaxies at similarly high spatial resolution. Each WFC frame targeting a high-latitude LBDS radio source contains typically two to six field galaxies with $18 \lesssim V \lesssim 22$ mag. These are generally not at the same redshift as the radio galaxies, which were *not* specifically selected in rich clusters. Measured spectroscopic redshifts for these field galaxies are in the range $z \simeq 0.1$–0.6. Another goal of this paper thus is to compare their sub-kiloparsec morphology and light profiles with those of the radio galaxies, and see if any field galaxies at the same redshift cause morphological distortions in the radio galaxy and possibly help fuel its radio source through interactions or mergers. An increasing database of field galaxies has been accumulated in particular by the *HST* Medium Deep Survey (MDS; Griffiths et al. 1993a, b; 1994, hereafter G94), which is of special interest, not only for the study of ordinary field galaxies, but also in the light of recent evidence for evolution of the cluster galaxy population from redshifts $z \simeq 0.4$–0.6 to the present (Dressler et al. 1993, 1994; McClure, Pierce, & Lavery 1993).

In § 2, we summarize all Cycle 1 WFC observations, their reduction, and deconvolution algorithms, and present the FOC/48 data, Multiple Mirror Telescope (MMT) spectroscopy, and United Kingdom Infrared Telescope (UKIRT) K-band images, in as much as these are not discussed in previous papers. In § 3, we discuss the reliability of the deconvolved WFC images, their light profiles, and fits of multicomponent galaxy models to the *aberrated* images. In § 4, we give the results for the *high-SB* radio and field galaxies with $z \lesssim 0.6$, which turn out to be mostly elliptical galaxies and S0s. In § 5, we further analyze deep WFC images of the young, compact radio galaxy at $z = 2.390$. In § 6, we present the results for the *lower SB* field galaxies, which have exponential disklike light profiles and are mostly early-type spirals out to $z \simeq 0.6$. Our conclusions are given in § 7. We use $H_0 = 50$ km s^{-1} Mpc^{-1} and $q_0 = 0.1$ throughout when quoting single physical values, and the plausible range $H_0 = 50$–100 and $q_0 = 0.0$–0.5 when considering ages and redshift of formation.

2. OBSERVATIONS AND PROCESSING

2.1. *WFC Observations*

Deep *HST* images were taken in 1991 September–December in the WFC filters F555W (V) and F785LP (I). Each individual exposure was maximally 20 minutes to reduce CR hits (see Windhorst, Franklin, & Neuschaefer 1994a, hereafter W94a) or 10 minutes for 53W044 to avoid saturation of the best PSF star (Keel & Windhorst 1993, hereafter KW93). A total of 8×10 minute exposures was taken for 53W044, 8×20 minute exposures for 53W046, and 12×20 minute WFC exposures for 53W002, all in both the V and I filters. Also, 8×13 minute FOC/F275W exposures were taken for both 53W044 and 53W046 to constrain their UV morphology and UV-optical colors. We placed all target radio galaxies in the center of chip WF1 since it is relatively clean cosmetically and has the highest quantum efficiency (QE) at the wavelengths of interest (Lauer 1989, hereafter L89; Griffiths 1990, hereafter G90). Details of the observations are given in Table 1.

2.2. *HST Data Processing*

A first pass through the calibration was done with the standard Wide Field/Planetary Camera (WF/PC) pipeline, details of which can be found in L89, W92, KW93, and W94c. Here we summarize the aspects important to understanding the reliability of the data presented in this paper.

After flat-fielding with the best available destreaked Earth flats, the signal-to-noise ratio (S/N) on the sky in the final stack is about 2%, but residual streak flat-field variations exist of

TABLE 1

HST WFC AND FOC/48 OBSERVATIONS OF LBDS RADIO GALAXIES

Name (Redshift) (1)	Detector/Filter (2)	Exposure (N_{exp} × s) (3)	Observation Date[a] (UT Start) (4)	Sky P.A. of *Y*-Axis[b] (5)	Sky Signal[c] (e^-) (6)	Sky Sigma[d] (e^-) (7)	Sky SB[e] (mag arcsec^{-2}) (8)	6 σ PSS[f] (mag) (9)	2 σ SBS[g] (mag arc sec^{-2}) (10)
53W044.....	F48/F275W	07 × 0770	1991 Aug 31	+124°	8.37	2.90	24.08	25.65	25.37
(0.311)	("UV")		(14:05:12)		[d = 7.55]	[2.89]			
	W1/F555W	08 × 0600	1991 Sep 01	+148°	510	60	23.39	24.83	26.75
	(*V*)		(02:10:39)		[p = 289]	[46]			
	W1/F785LP	08 × 0600	1991 Dec 16	+228°	528	52	21.95	22.87	25.47
	(*I*)		(15:54:39)		[p = 289]	[47]			
53W046.....	F48/F275W	07 × 0807	1991 Aug 26	+130°	9.20	3.18	24.26	25.60	25.32
(0.528)	("UV")		(09:46:30)		[d = 8.47]	[3.03]			
	W1/F555W	08 × 1200	1991 Aug 27	+152°	428	66	23.42	25.42	27.34
	(*V*)		(06:02:39)			[46]			
	W1/F785LP	08 × 1200	1991 Dec 16	+228°	473	52	21.97	23.44	26.04
	(*I*)		(09:34:39)			[46]			
53W002.....	W1/F555W	12 × 1200	1991 Oct 25	+095°	788	73	23.20	25.60	27.52
(2.390)	(*V*)		(06:18:39)			[58]			
	W1/F785LP	12 × 1200	1991 Oct 26	+095°	571	68	22.20	23.65	26.25
	(*I*)		(04:48:39)			[56]			

[a] Date of *HST* observation and UT start time of first exposure. All subsequent *HST* exposures were done *without* orbital gaps.

[b] Sky P.A. (in degrees from north through east) of the detector's *Y*-axis (for CCD 1 in case of WFC), corrected for the *HST* spacecraft orientation.

[c] Total sky signal (in e^-) of the exposure stack. Only for the shorter WFC exposure times of 53W044, a nonzero preflash (p = 5.0 DN per exposure) was needed. (This is indicated on the second line—in brackets—as is the rather low FOC/48 dark current of d = 0.0014–0.0015 e^- pixel^{-1} s^{-1}, which is similar to the 0.00138 e^- pixel^{-1} s^{-1} by Bertola et al. 1993).

[d] Observed sky sigma (in e^-) in the image sum. The number in brackets on second line gives the expected sky sigma from the CCD equation, with an average WFC gain of 7.2 e^- DN^{-1}, observed read noise (including A/D problems) of 14.2 e^-, and WFC dark current d = 0.0074 e^- pixel^{-1} s^{-1}. The ~3%–7% WFC flat-field (destreaking) errors (and some residual even-odd column problems) cause the ~1.2 times larger observed sky sigma.

[e] Sky surface brightness (in mag arcsec^{-2}) resulting from cols. (3) and (6). For cols. (8), (9), and (10), we used the magnitude zero points described in § 2. For CCDs other than WF1, these numbers may differ by ~0.1 mag.

[f] Six σ point-source sensitivity (in magnitudes, including spherical aberration losses) resulting from cols. (3) and (7).

[g] Two σ surface brightness sensitivity (in mag arcsec^{-2} over a 1.0 arcsec^2 area) resulting from cols. (3) and (7) and the average WFC scale of 0.″1016 pixel^{-1}.

order 3%–7%. Although we detect these, they do not generally prohibit analysis of object light profiles, since the sky level in our North Ecliptic Pole (NEP) images is so low (see below), and most objects are smaller than the typical streak pattern. Next, we carried out the following steps:

1. Check the coregistration of the WFC images as in W92. The *V* and *I* stacks on 53W044 and 53W046 were taken 3.5 months apart, and thus have considerably different *HST* spacecraft orientation angles. No attempt was made to rotate them onto one coregistered frame, since rotation of undersampled images would increase the noise, and the objects of interest were bright or red enough that co-adding the *V* and *I* images would not reveal any extra morphological features not already seen in the *I* band.

2. Remove the myriads of CR hits in our images, since these can be quite damaging to deconvolution results. Windhorst et al. (1993a, hereafter W93a) and Windhorst, Franklin, & Neuschaefer (1994a, hereafter W94a) show that the fraction of pixels affected by CRs is substantial and that CRs are most properly removed in the image-stacking phase. W94a therefore developed and extensively tested an algorithm that iteratively determines clipped averages for each pixel over all 8–12 exposures. We performed their two-sided 2 σ clipping to avoid bias in the sky level. If the measured σ-value per pixel differed from Poissonian by more than 15%–20%, it was set to the Poissonian value (see W94a for details).

3. Find hot pixels from step 1 and the STScI data quality maps. The pixels are corrected through an iterative nonlinear interpolation routine that to first order preserves local SB. Deconvolution algorithms would otherwise diverge on those pixels. This cannot be easily avoided by masking the hot pixels (i.e., leaving their value as is, but ignoring them in the analysis, as is done with surface photometry fits), since (nearly) photon-preserving deconvolution algorithms assume that all real flux is actually in the image. Progress has recently been reported in this area through the use of dynamic pixel weighting (K91; White 1993).

4. Measure the *HST* sky brightness for these fields. From Hunter et al. (1992) and Holtzman et al. (1991), we derive the following instrumental constants (for 1.0 DN s^{-1}) for the center of WF1 (using flats with neutral density filter F122W): 22.87 ± 0.07 mag in F555W and 21.52 ± 0.05 mag in F785LP. The zero points for the other chips are within ~0.1 mag of these numbers and are given in Hunter et al. (1992). The FOC/48 zero point is bootstrapped in § 2.5. At the high ecliptic latitude of our Hercules survey field, the observed *HST* sky brightness is $m_{2750} \simeq 24.16 \pm 0.13$ mag arcsec^{-2}, $V \simeq 23.34 \pm 0.12$ mag arcsec^{-2}, and $I \simeq 22.04 \pm 0.14$ mag arcsec^{-2}. The resulting 2 σ SB sensitivity (in a 1.0 arcsec^2 detection cell) is ~25.3 mag arcsec^{-2} in m_{2750}, ~26.7–27.5 mag arcsec^{-2} in *V*, and ~25.5–26.3 mag arcsec^{-2} in *I*. The 6 σ point-source sensitivity (with spherical aberration) is ~25.6 mag in m_{2750}, ~24.8–25.6 mag in *V*, and ~22.9–23.7 mag in *I* (see Table 1).

5. Where needed, a two-dimensional (bicubic) spline surface was subtracted from the flat-fielded images to remove remaining gradients to ~1% of sky. An independent check of the error in the subtracted sky values was made by verifying that the resulting WFC *V* and *I* magnitudes (corrected for the small color terms of Harris et al. 1991) differed from the measured ground-based value (W91) by less than twice their combined error. The subtracted modal-sky values are thus appropriate for construction of light profiles presented in §§ 4–6.

2.3. *Constructing Sky Flats from Deep WFC Images*

WFC super–sky flats are now available from the *HST* MDS (G94; Ratnatunga et al. 1984). We caution that our three deep Cycle 1 images in Hercules are not appropriate to include in WFC sky flats because (1) all radio galaxies were placed in the center of WF1; (2) the images were deliberately *not* jittered to allow better CR removal, and (3) the NEP sky is so dark that the sky signal is too low for super–sky flats.

2.4. *Deconvolution of the WFC Images*

2.4.1. *Application of σ-CLEAN and the Multiresolution CLEAN*

The images were deconvolved with the σ-CLEAN algorithm, as described by Keel (1991) and KW93. Both WFC simulations and our experience with real WFC data show the *HST* images can be deconvolved to nearly the diffraction-limited performance (or the Nyquist limit), but with limited dynamic range (16–25 dB).

To improve the S/N at low spatial frequencies without a noise penalty at high spatial frequencies, we used a modification of the multiresolution CLEAN (MR-CLEAN) method of Wakker & Schwarz (1988, hereafter WS). The details of this hybrid CLEAN are described by KW93. In summary, WS smooth both image and PSF with a Gaussian (with FWHM $\simeq$ the object's FWHM) to produce a low spatial frequency image. This is subtracted from the original image, so that the difference image contains primarily high spatial frequencies. Both these images are then deconvolved separately with their individual PSFs, as appropriate. This MR-CLEAN process reduces the noise that a single CLEAN would introduce at high spatial frequencies, since CLEAN overinterprets the low spatial frequencies as unphysical point sources.

Note that the radio astronomers' difference image used in MR-CLEAN is allowed to go negative in deep interferometer maps—especially in the presence of marginal cosmic background radiation (CBR) fluctuations—because the Parseval relation requires the total interferometer flux to be zero (e.g., W93b). On the contrary, we do not deconvolve the difference WFC image with a difference PSF, but with the original PSF, since any real photon flux in the difference image must be positive, and still bear the signature of *HST*'s original (i.e., not difference) PSF. For further details on MR-CLEAN, see W92, KW92, and W94c.

2.4.2. *Application of the Lucy Method*

We also deconvolved our images with the Lucy (1974) algorithm as implemented within STSDAS, using a range of 20–100 iterations. We consistently find that fewer iterations do not produce convergence in galaxy wings, while many more interations produce more plausible results in the galaxy cores, but sometimes overshoot in the galaxy wings, and in any case produce more noise. Note that the σ-CLEAN algorithm preserves photons by definition, since for every subtracted scaled version of the PSF the same amount of flux is restored back into the image, while Lucy nearly preserves photons, unless one pushes the algorithm too far. In §§ 4–6, we do not find significantly different image structures between Lucy and MR-CLEAN, except that MR-CLEAN yields somewhat sharper object cores, as expected from the performance of both algorithms at the various spatial frequencies. While the Lucy and σ-CLEAN algorithms operate quite differently, they give consistent results within the limited dynamic range of our data. KW93 show that Lucy performs better in the low-SB outskirts of galaxies, while MR-CLEAN gives more realistic core fluxes in a limited number of iterations (see also W92). However, there is a large region of considerable overlap, where both algorithms produce consistent light profiles within the statistical (and external) errors of the data (see §§ 4–6).

2.4.3. *Effects from the FOV-dependent PSF*

The $V = 19.4$ mag LBDS radio galaxy 53W044 is 5″.5 (55 WFC pixels) away from a $V = 18.1$ mag star (its MMT spectrum classifies it as a G9 dwarf; see § 2.5.2). This is our best available PSF star, which we used for all objects in the center of WF1. Because the *HST* PSF is strongly field dependent, we limit simultaneous deconvolution to subimages not exceeding 120 × 120 pixels, using the closest PSF star (usually within 50, but sometimes 170, pixels) with the highest S/N. For a few galaxies, no suitable PSF star was available, so we constructed a library of artificial PSFs with the TinyTIM package as implemented under STSDAS and verified that our observed PSF stars deconvolved into δ-functions with the TinyTIM model (within typically $\lesssim$16–25 dB). For further discussion of the field dependency of the PSF, see W94c.

2.4.4. *Effects from the Time-dependent PSF and Spacecraft Jitter*

During the 3.5 month interval between our first and last Cycle 1 observations, focus changes of the *HST* Optical Telescope Assembly (OTA) were $\lesssim 6$ μm (Hasan & Burrows 1993). The PSF may change significantly on longer timescales, because of OTA outgassing and of deliberate focus changes applied by STScI to compensate for this. Over this 3.5 month interval, the $\lesssim 6$ μm focus change and the resulting PSF changes do not limit the dynamic range of the deconvolutions as much as the field dependence of the PSF (§ 2.4.3). To deconvolve images with PSFs taken more than 3 months earlier or later, we have been building up a large time-dependent PSF library from our Cycle 1–3 WFC images in the MDS (Griffiths et al. 1993a, 1994; W94c). Another effect is difference in spacecraft jitter between the object and PSF image, if the two come from different WFC exposures. In our WFC images, we find the spacecraft jitter in coarse lock to be $\lesssim$0″.03–0″.04, i.e., much less than the WFC pixel size (0″.1016) and hardly noticeable when added in quadrature (except in the cores of heavily saturated stars; see W94a). Differential spacecraft jitter thus also does not limit the dynamic range of the deconvolutions as much as the field dependence of the PSF (§ 2.4.3).

2.5. *FOC/48 Observations of Radio Galaxies with z = 0.3–0.6*

2.5.1. *FOC/48 Images*

We also took FOC/48 exposures in the F275W filter for 53W044 (7 × 770 s) and for 53W046 (7 × 807 s) to constrain their mid-UV flux and morphology (see Table 1). For six out of eight 53W046 images, and all seven 53W044 images, Fine Guidance Sensor (FGS) finelock was maintained. Using the bright star near 53W044 as reference, the σ in each coordinate was 0.17 FOC/48 pixel, or 0″.007. Since these numbers are dominated by photon statistics in the star image, we made no shifts before co-adding the FOC exposures. The stellar brightness was consistent with the relative exposure times of each image. The original 512 × 1024 FOC stacks have 0″.086 × 0″.043 pixels and were expanded with the IRAF task "dezoomx" to 1024 × 1024 pixels of 0″.043 × 0″.043 in a photon-preserving way (this decreases the image σ per output pixel by $\sqrt{2}$, for which we corrected in Table 1).

The FOC/48 images for all objects have a gradient in the

background of about 15% along the Y-axis across the inner half of the FOC frame. Presumably, this is due to remaining FOC dark current. The subtracted FOC/48 dark current is 0.0014–0.0015 e^- pixel^{-1} s^{-1}, and comes primarily from internal thermionic emission rather than from solar particles. Bertola et al. (1993) found a similar low FOC/48 dark current of 0.00138 e^- pixel^{-1} s^{-1}. We fitted a bicubic spline surface to the inner 512 × 512 pixels of each clipped image stack and subtracted this from the image.

2.5.2. *Bootstrap of the In-Flight FOC/48 Zero Point*

The FOC/48 does not have an *on-orbit* calibration. However, Sparks (1992) found that the on-orbit FOC/96 calibration was always within 20%—and usually within 10%—of the prelaunch FOC Handbook values. Hence, we used Sparks's FOC/96 on-orbit calibration and the ratio of FOC/48 and FOC/96 preflight calibrations (Paresce 1990, 1992) to derive a first-order zero point for the FOC/48. In F275W, the measured on-orbit FOC/96 + F275W throughput is 6.7% less than the preflight value. For 1.00 count s^{-1}, the latter is 1.085×10^{-17} ergs cm^{-2} s^{-1} Å^{-1} (Paresce 1990), or $m_{2750} = 21.38 \pm 0.15$ mag. The on-orbit FOC/48 zero point is then $1.085 \times 10^{-17}/0.933 = 1.163 \times 10^{-17}$ ergs cm^{-2} s^{-1} Å^{-1}, or $m_{2750} = 21.30 \pm 0.15$ (the error is from the FOC/96 calibration), or $AB_v = 22.73$ mag (adopting AB_v (α Lyr) = 1.49 mag from Oke & Gunn 1982, and m_λ (2750 Å, α Lyr) = 0.06 mag from the Appendix of W91).

Both the 53W044 and 53W046 FOC/48 images contained bright stars (53W044* and 53W046*; see Table 2), whose spectral type could be determined from high-quality MMT spectra (§ 2.7). This allowed us to refine the absolute FOC/48 zero point as follows. Their line strengths were compared with stars of known MK type from the Jacoby, Hunter, & Christian (1984) and the Wu et al. (1991) spectral atlases, and are most consistent with G9 ± 2 and G6 ± 2, respectively. We constructed composite spectra using the optical MMT spectra and the typical *IUE* spectra for G6–9 dwarfs (V = 18–19 mag stars at this latitude should be dwarfs), scaled to their appropriate UV − V color. There is a faint star ($V = 22.13 \pm 0.10$ with $V-K = 4.07$ mag from the UKIRT K-band images; § 2.7) a few arcseconds away from the star 53W046* (see Table 2). This M2 dwarf is too faint in the optical/UV to affect the UV flux or red leak of 53W046* significantly. As red leak we took the predicted fraction of counts for $\lambda \gtrsim 3077$ Å (the nominal F275W half-power point), multiplying the star's photon spectrum by the most recent FOC/48 + F275W throughput curve kindly supplied by W. Hack at STScI. The G9 star 53W044* has a redleak of 49% ± 5%, and the G6 star 53W046* has 56% ± 5% (note that these fractions are the reverse of what one expects for their spectral types, but these are uncertain by ±1 spectral class, and the predicted red leak by ±5%). From Burstein & Heiles (1982), we find $E_{B-V} = 0.021$ mag for the Hercules LBDS field in which the 53W sources are located. From Seaton (1979), we find modest Galactic extinction from 2750 Å to 2.2 μm, which is listed at the bottom of Table 2. We corrected all observed magitudes in Table 2 accordingly, except the Mayall 4 m U magnitudes for 53W044 and 53W046 of KKW that were already extinction corrected.

The observed red leak and extinction-corrected count rate of 53W044* is 2.13 ± 0.26 counts s^{-1} (the error comes primarily from the sky subtraction underneath the large FOC star image). Following § 6.0 in the Cycle 2 FOC Handbook (Paresce 1992) with QT = 0.026 for FOC/48 + F275W and $\Delta\lambda = 654$ Å, this count rate corresponds to a 2750 Å flux of 2.48×10^{-17} ergs cm^{-2} s^{-1} Å^{-1}. The red leak and extinction-corrected count rate predicted from the scaled MMT + *IUE* spectrophotometry is 2.30×10^{-17} ergs cm^{-2} s^{-1} Å^{-1}, so that an observed red leak and extinction-corrected flux of 1.00 counts s^{-1} would correspond to 1.08×10^{-17} ergs cm^{-2} s^{-1} Å^{-1}, or an FOC/48 + F275 zero point of $m_{2750} = \mathbf{20.38} \pm 0.16$ mag. For 53W046* we similarly observed a count rate of 1.28 ± 0.18 counts s^{-1} or 1.49×10^{-17} ergs cm^{-2} s^{-1} Å^{-1} with 56% red leak, while we predict 1.45×10^{-17} ergs cm^{-2} s^{-1} Å^{-1}, so that its FOC/48 + F275 zero point is $m_{2750} = \mathbf{20.33} \pm 0.19$ mag. The observed B and V photometry in Table 2 combined with the model 2750 − B and 2750 − V colors of Bruzual (1981, 1983, his Table 47) suggest—within the errors—predicted 2750 Å fluxes for both stars that are similar to those derived above from the MMT + *IUE* spectrophotometry.

The two independent FOC/48 zero points are within the errors consistent with the preflight FOC/96 measurement converted to FOC/48 in-flight with the measured FOC/96 in-flight/preflight ratio. Weighting these three independent measurements with their formal errors, we find as best average zero point for the bootstrapped on-orbit FOC/48 + F275W sensitivity: $m_{2750} = \mathbf{21.34 \pm 0.09}$ **mag for 1.00 count s^{-1}**. This adopted zero point yields a UV night-sky brightness at 2750 Å of 24.2 ± 0.2 mag arcsec^{-2} (the error comes mostly from the subtracted FOC/48 dark current of 0.00145 e^- pixel^{-1} s^{-1}. This is only marginally brighter than O'Connell's (1993) measured value of 24.6 mag arcsec^{-2} with the Ultraviolet Imaging Telescope (UIT) at 2800 Å. Note also that our definition of UV magnitudes is similar to that of Smith et al. (1992) on UIT images, who defined $m_{2490} = -2.5 \log F_\lambda - A_\lambda - D$ with $D = 21.1 \pm 0.10$ mag. Using $A_{2750} = 0.13$ mag for Hercules, our bootstrapped FOC/48 zero point corresponds to a (dereddened) $D = -(21.34) - 2.5 \log (1.125 \times 10^{-17}$ ergs cm^{-2} s^{-1} Å^{-1}) = 21.03 ± 0.09 mag, consistent with the Smith et al. definition.

2.5.3. *Analysis of the FOC/48 Images*

Convolving the FOC images with a $\lesssim$0.″2 FWHM Gaussian, we clearly detected 53W044, but only barely 53W046. No prominent point sources are visible in the galaxies from the F275W images, suggesting that the mid-UV flux of these weak radio galaxies is *not* primarily caused by nonthermal emission. The FOC stack of 53W044 shows signal above 2 σ in 16 contiguous 50-pixel blocks around the galaxy position, with a total flux of 0.931 counts s^{-1}, corrected for foreground extinction ($A_\lambda = 0.13$) and the expected 24% red leak calculated by KW93 for 53W044's spectrum at $z = 0.311$ (see Fig. 1). Contrary to the situation for low-redshift galaxies, the red leak for early-type galaxies with $z \gtrsim 0.3$ in FOC/48 + F275W is rather modest, since the H and K break is beyond 5100 Å, where the FOC/48 + F275W throughput rapidly declines (it drops to zero rapidly beyond 6000 Å). 53W044's count rate corresponds to 1.08×10^{-17} ergs cm^{-2} s^{-1} Å^{-1}, or $m_{2750} = 21.43 \pm 0.17$. The best-fit Bruzual (1983, Tables 51B and 52B; 1988) model to a galaxy at $z = 0.311$ with colors as in Table 2 has $\mu \simeq 0.40$ (for $H_0 = 50$, or $\mu \simeq 0.65$ for $H_0 = 100$), and predicts 27 − B and 27 − V colors that imply $m_{2750} = 21.52 \pm 0.16$ mag, consistent with the observed value, given the uncertainties in the models and ground-based measurements. 53W044 has $V = 19.4$ mag or F_λ (5500 Å) = 6.21×10^{-17} ergs cm^{-2} s^{-1} Å^{-1}. At $z = 0.311$, the observed V filter has mean rest-frame wavelength of 4200 Å (including the 4000 Å break on one side),

TABLE 2

AVAILABLE MULTIBAND PHOTOMETRY OF *HST* RADIO GALAXIES AND SURROUNDING OBJECTS

Name[a] (1)	z (2)	m_{2750}[b] (mag) (3)	U[c] (mag) (4)	B (mag) (5)	V (mag) (6)	R (mag) (7)	I (mag) (8)	g (mag) (9)	r (mag) (10)	i (mag) (11)	J (mag) (12)	H (mag) (13)	K (mag) (14)	Classification (15)
53W044	0.311	21.43	21.45	20.88	19.38	18.01	17.19	...	...	...	16.40	15.28	14.63	S0 radio galaxy (KW93)
		(0.17)[d]	(0.20)	(0.15)	(0.10)	(0.10)	(0.10)				(0.19)	(0.07)	(0.08)	
53W046	0.528	22.13	22.24	22.29	21.13	19.41	18.49	...	...	...	17.27	16.46	15.94	gE radio galaxy
		(0.21)	(0.20)	(0.18)	(0.10)	(0.11)	(0.10)				(0.10)	(0.08)	(0.12)	
53W002	2.390	...	>23.0[e]	23.13	22.95	22.45	22.00	22.81	22.76	22.67	20.70	19.84	19.07[f]	Radio galaxy (W91)
				(0.17)	(0.11)	(0.15)	(0.12)	(0.09)	(0.09)	(0.10)	(0.28)	(0.29)	(0.30)	
53W002a	0.58	...	>23.0	23.23	22.82	20.92	20.26	22.79	21.58	21.14	19.44	18.22	17.52	Ell field galaxy
				(0.19)	(0.11)	(0.15)	(0.10)	(0.10)	(0.06)	(0.06)	(0.10)	(0.10)	(0.21)	
53W044a	0.131	...	...	18.54	17.70	16.86	16.43	...	...	...	...	...	...	Early-type Spiral + Bar
				(0.15)	(0.10)	(0.10)	(0.10)							
53W044b	0.199	...	...	20.58	19.51[g]	18.65	18.14	...	...	...	...	...	...	Late-type Spiral
				(0.15)	(0.15)	(0.10)	(0.10)							
53W044c	...	21.88	...	22.19	22.27	21.44	21.57	...	...	...	...	...	18.58	UV galaxy (KW93)
		(0.21)		(0.20)	(0.11)	(0.14)	(0.11)						(0.30)	
53W044*	0.000	20.52	...	18.62	18.06	17.20	17.06	...	...	...	...	...	16.33	PSF-star (G9 dwarf) for WF1 center
		(0.12)		(0.20)	(0.10)	(0.10)	(0.10)						(0.14)	
53W046*	0.000	21.07	...	19.36	18.81	18.07	17.89	...	...	...	...	...	17.21	Brightest of double star (G6 + M2 dwarfs)
		(0.12)		(0.15)	(0·10)	(0.10)	(0.10)						(0.19)	
53W002b	0.193	...	22.52	21.51	20.71	...	18.99	20.71	20.05	19.81	...	...	...	Early-type Spiral + Bar
			(0.37)	(0.12)	(0.10)		(0.10)	(0.05)	(0.05)	(0.05)				
53W002c	0.273	...	20.86	20.56	19.84	...	18.00	19.89	19.14	18.88	...	...	...	Early-type Spiral + Bar?
			(0.24)	(0.10)	(0.10)		(0.10)	(0.05)	(0.05)	(0.05)				
53W002d	0.275	...	...	...	19.73	...	17.69	19.78	18.92	18.61	...	...	...	Early-type Spiral + Companion
					(0.10)		(0.10)	(0.05)	(0.05)	(0.05)				
53W002e	0.528	...	...	...	20.59	...	18.48	20.59	19.72	19.37	...	...	...	Early-type Spiral + Companion
					(0.10)		(0.10)	(0.05)	(0.05)	(0.05)				
A_λ (mag)		0.13	0.10	0.088	0.067	0.05	0.03	0.08	0.05	0.04	0.02	0.01	0.01	Adopted extinction for $E_{B-V} = 0.021$

[a] 53W044, 53W046, and 53W002 indicate LBDS radio galaxies. The other object names indicate several surrounding field galaxies also detected in the WFC frames. 53W002a is the same as Object 6 of W91.

[b] m_{2750} corrected for the following FOC/48 + F275W red leaks (see KW93): 24% for 53W044 at $z = 0.311$, $\sim$ 12% for 53W046 at $z = 0.528$ and for the UV galaxy 53W044c (unknown z but flat SED), 49% for the G9 star 53W044*, and 56% for the G6 star 53W046*.

[c] All fluxes, including V and I, are aperture magnitudes grown to nearly total following W91 and corrected for Galactic extinction as described in § 2. *Model* V and I magnitudes for galaxies are given in Table 3.

[d] The listed optical/IR errors follow from adding in quadrature the objects' inverse signal-to-noise ratio and the errors in the sky subtraction, in the FOC/48 + F275W red leak, and in the magnitude zero point. The latter are $\sim$0.09 mag in m_{2750}, 0.20 mag in U, 0.10–0.15 mag in B, 0.10 mag in V, R, and I, and $\lesssim$0.05 mag in Gunn *gri* and in Johnson *JHK*.

[e] All upper limits are 2 σ.

[f] Subtracted from the observed $K = 18.61 \pm 0.17$ the $\sim$35% contribution of redshifted Hα (Eales & Rawlings 1993).

[g] 53W044b is on the pyramid edge of the V image with about 19.68 ± 0.10 mag of its flux on WF1 and 21.76 ± 0.10 mag on WF2. Its total V magnitude (= 19.51)—corrected for the $\sim$2% light lost at the pyramid edge—is uncertain by $\pm$0.15 mag, but quite consistent with the extrapolated model value of Table 3.

so that the emitted-frame V-band flux will be ~ 2.1 times higher for a representative elliptical galaxy (see Fig. 1). This gives an F_λ ratio in the emitted frame (corrected for foreground reddening) of $F_\lambda\,(2100)/F_\lambda\,(V) = 0.099$, or -1.00 dex. This is consistent with the 2000–5500 Å flux ratio of the four nearby early-type radio galaxies observed by *IUE* by Keel & Windhorst (1991, Fig. 7). Both these best-fit Bruzual models and this rather red $2100 - V$ color are equivalent to a ~ 5 Gyr stellar old population at $z = 0.311$ (see also KW93).

After convolving the 53W046 image stack with a 0.″25 Gaussian, a faint 2–3 σ object is visible at the position corresponding to the optical coordinates of 53W046. Its F275W

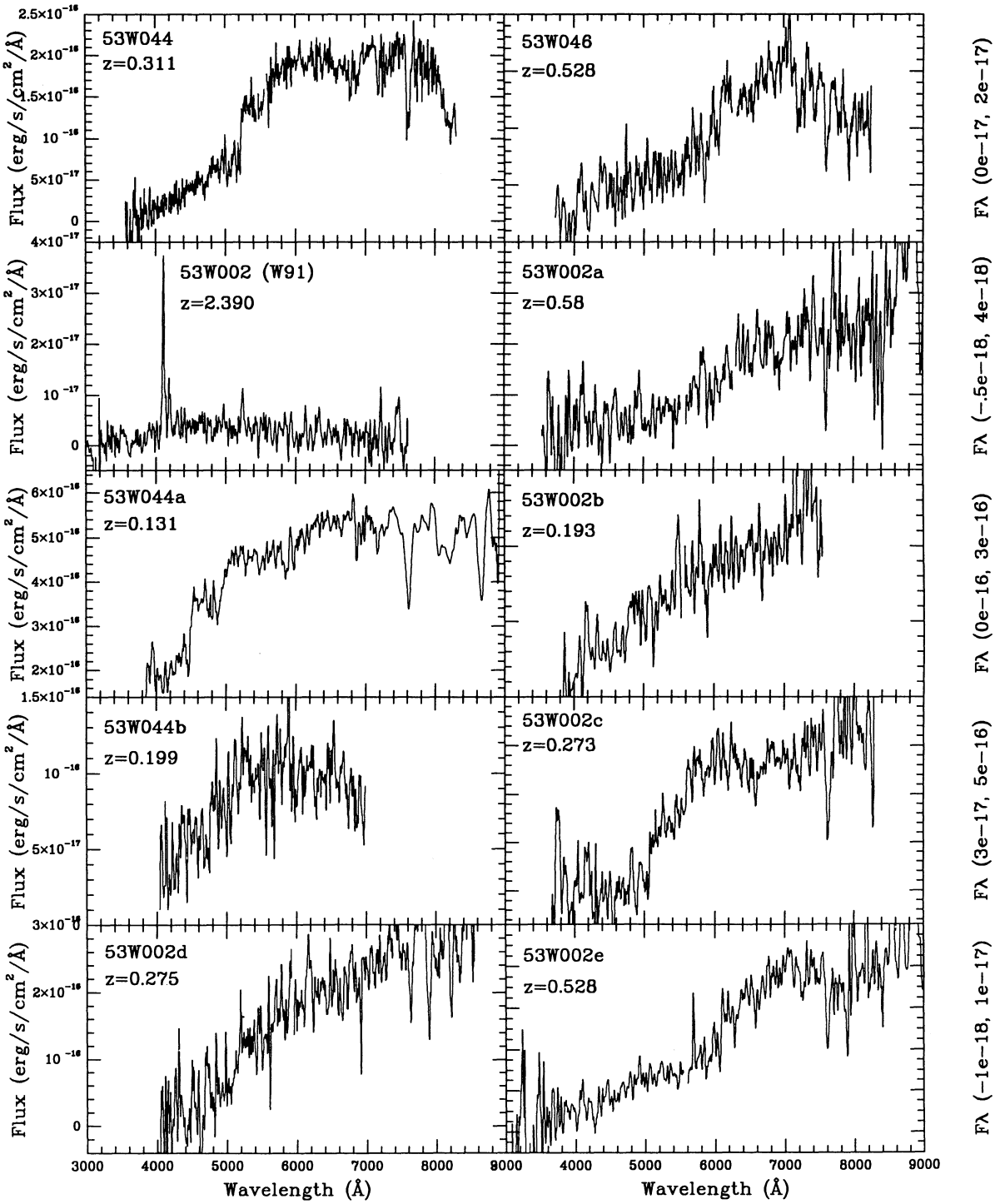

FIG. 1.—MMT spectra for the three radio galaxies and seven field galaxies discussed in the text. Spectra for the radio galaxy 53W002 were done with the MMT Big Blue Spectrograph (see W91) and a 2″ × 3″ aperture. The radio galaxies 53W044 and 53W046 were done with the MMT Red Spectrograph and a 1.″5 × 180″ long slit. All other objects were done with the MMT Red Spectrograph and the 2″ × 20″ multislit assembly. All spectra have been fluxed.

count rate is about a factor 1.9 lower than that of 53W044, and its extinction and red leak–corrected flux is about 5.6×10^{-18} ergs cm^{-2} s^{-1} Å^{-1}. Both the FOC/48 exposures on 53W044 and 53W046 will be further analyzed in combination with MMT spectrophotometry (3100–8250 Å) and FOS/G190H spectroscopy (1550–2350 Å) to trace the UV upturn of early-type galaxies with cosmic time (W94b; Pascarelle et al. 1994).

2.6. *MMT Spectroscopy of HST Radio and Field Galaxies*

Ground-based spectrophotometry has been obtained with the MMT Red Spectrograph for several LBDS radio galaxies (see also W91; W94b). We also obtained MMT spectroscopy to determine redshifts for the field galaxies seen in our Cycle 1 WFC images (with $V \lesssim 22.5$ mag). Details of the MMT observations and reduction are given by W94c. The fluxed MMT spectra are displayed in Figure 1.

2.7. *UKIRT K-Band Imaging of the Compact HST Galaxies*

We used the 62 × 58 pixel InSb array camera IRCAM (McLean et al. 1986) on the 3.9 m UKIRT to image the three compact LBDS radio galaxies and their immediate surroundings in the K band. The camera was operated in the 0.″62 pixel^{-1} mode, and the typical K-band seeing FWHM was 1.″0–1.″1.

The observing and reduction procedure was as in Dunlop & Peacock (1992). The result of this "dithering" procedure is an expanded 54″ × 52″ image in which only the central 22″ × 20″ received the full 27 minutes of exposure time. All sky estimates were therefore made very close to the object, avoiding any unevenly exposed areas. In photometric nights, we found an instrumental constant of $K = 20.32 \pm 0.02$ for 1.0 DN s^{-1}.

The high-redshift object 53W002 is sufficiently small that we could produce a good median-filtered sky flat from on-source exposures. For 53W002, one 27 minute K-band mosaic was taken in 1990 October, and a second one in 1992 June. The extrapolated "total" magnitudes are $K = 18.50 \pm 0.18$ and 18.40 ± 0.22, respectively. In a 3″ diameter aperture the average $K = 19.1 \pm 0.2$, and in a 4″ aperture $K = 18.6 \pm 0.15$, somewhat brighter than the shallower Palomar 200 inch (5.08 m) IR-array measurement of W91, who measured $K = 19.2 \pm 0.3$ in a 4″ aperture and noticed that the K-band growth curve of 53W002 was only slowly converging. We note that Hα will be in the middle of the K band, although the IR spectroscopy of 53W002 by Eales & Rawlings (1993) does not show a strong enough detection of Hα to affect the K-band flux significantly. In their 3.″1 aperture, our $K \simeq 19.1$ magnitude implies an equivalent width for Hα + [N II] of 0.075 μm (or 221 Å in the emitted frame), so that Hα line emission contributes only $\lesssim 16\%$ of the continuum K-band flux. As shown in § 5.1, the nonstellar component in 53W002's spectrum constitutes $\lesssim 30\%$ of the total continuum, consistent with the Eales & Rawlings IR spectrum given their low S/N. Our measured "total" K-band flux of 18.5 ± 0.2 mag then implies a stellar K-band magnitude of 19.0 ± 0.3, consistent with the $K = 19.2 \pm 0.2$ derived for the stellar population by W91 from their Palomar K-band images.

The reduction procedure for the 53W044 and 53W046 K-band exposures was similar to that described above, with the exception that only eight off-source images were used to produce the median-filtered sky flat, because of the larger object extent. For 53W044, we obtained two, and for 53W046 one 27 minute K-band mosaic in 1992 June. The UKIRT K-band magnitudes in Table 2 are consistent with the aperture photometry of Thuan et al. (1984) for these galaxies. For object 53W002a at $z = 0.58$ (Object 6 of W91), we found $K = 17.52 \pm 0.21$, consistent with the Palomar $K = 17.53 \pm 0.20$ mag of W91, who classified this object as a star, since it was not significantly extended on their Palomar 200 inch Four-Shooter and IR images (which had FWHM ~ 1.″1–1.″6). However, our *HST* images of § 4.2 clearly show that it is a compact galaxy. Its MMT redshift is $z = 0.58$ (see § 4.3).

2.8. *Twelve-Band m_{2750} UBVRIgriJHK Photometry and Its Zero Points*

CCD photometry in Gunn *gri* plus Johnson *UB*, and bootstrap of the Johnson *UB* zero points, was presented by W91 for the 53W002 field. The *JHK* photometry with the Palomar 200 inch IR array is also described by W91. Calibrated photographic Mayall 4 m photometry in U^+ J^+ *FN* for the entire Hercules field was presented by KKW, and converted to *UBRI* using the transformations of W91. For 53W044 and 53W046, we obtained additional Steward 90 inch (2.3 m) CCD photometry in Johnson *BR* on 1990 June 15–18. While the *R*-band images were photometric, part of the *B*-band zero points had to be bootstrapped as described in W91.

Johnson *VI* photometry comes from the raw WFC images, using the zero points of Hunter et al. (1992) and the small color transformations of Harris et al. (1991). Aperture V and I magnitudes were grown to "nearly total" and are given in Table 2 (this includes the PSF wings as much as allowed by remaining gradients in the subtracted WFC sky; see § 2.2). Extrapolated model galaxy V and I magnitudes from §§ 4–6 are given in Table 3. The average difference between the nearly total and extrapolated model magnitudes for the 10 galaxies is remarkably small: $\pm 0.04 \pm 0.04$ (m.e.) mag in V and -0.01 ± 0.03 mag in I, showing that remaining aperture effects due to the large *HST* PSF must indeed be small (because we grew the apertures until the integral converged or ran into a neighbor).

Our 12-band photometry has zero points accurate to ~0.09 mag in m_{2750}, 0.20 mag in U, 0.10–0.15 mag in B, 0.10 mag in V, R, and I, and $\lesssim 0.05$ mag in Gunn *gri* and in Johnson *JHK*.

3. INTERPRETING THE RAW AND DECONVOLVED WFC IMAGES

In this section, we summarize the construction of isophotal galaxy fits and their reliability, as well as that of the deconvolved images by comparing the Lucy and MR-CLEAN profiles, in so far as important to understand the new results in §§ 4–6. For further details, we refer to KW93 and W94c.

3.1. *Isophotal Fits*

We made ellipse fits to the galaxy SB profiles with the STSDAS "isophote" package, yielding as best-fit parameters: central pixel values (X_0, Y_0), ellipticity e, position angle P.A. (with respect to the positive Y-axis of each WFC CCD, but corrected for the *HST* spacecraft orientation to get true sky position angles in Table 2 and Figs. 2–4), and the mean SB in V and I as a function of the semimajor axis a (or $a^{1/4}$) of successive elliptical annuli.

3.2. *Reliability of the Isophotal Fits*

The question if the Lucy and MR-CLEAN profiles are reliable at the faintest SB level critically depends on the dynamic range of the deconvolved image (as limited by the proximity of the best available PSF; § 2.4), the quality of the flat fields

TABLE 3

HST ASTROMETRY AND PHOTOMETRY OF DISTANT RADIO AND FIELD GALAXIES WITH MMT REDSHIFTS

Name[a] (1)	z (2)	CCD[b] (3)	$X(I)$[c] (pixels) (4)	$Y(I)$[c] (pixels) (5)	R.A.[d] (J2000) (6)	Decl.[d] (J2000) (7)	r_e/r_s[e] (8)	P.A.[f] (9)	e[g] $(1 - b/a)$ (10)	B/D[h] (I) (11)	V_{int}[i] (mag) (12)	I_{int}[j] (mag) (13)	SB_V (mag arcsec^{-2}) (14)	SB_I (mag arcsec^{-2}) (15)
53W044	0.311	W1	0423	0394	17^{h}17^{m}36^s.751	+50°03′04″.23	1″.2/1″.9	055°	0.27/0.23	5.3	19.42	17.14	18.11	16.23
					0.084	0.37								
53W046	0.528	W1	0420	0399	17 17 53.268	+50 07 51.52	0.9/1.0	148	0.25/0.18	>10	20.96	18.63	19.41	17.08
					0.045	0.08								
53W002	2.390	W1	0411	0397	17 14 14.734	+50 15 29.99	1.1/...	105	0.21/...	>10	22.98	22.01	20.34	20.24
					0.023	0.06								
53W002a	0.58	W1	0440	0371	17 14 14.462	+50 15 33.14	0.6/0.6	068	0.16/0.21	>10	22.69	20.32	22.07	19.18
					0.003	0.03								
53W044a	0.131	W1	0211	0159	17 17 36.842	+50 02 31.94	1.7/2.0	083	0.46/0.20	2.5	17.89	16.47	17.94	16.35
					0.026	0.19								
53W044b	0.199	W1	0741	0102	17 17 32.174	+50 03 02.60	1.8/1.7	111	0.51/0.41	0.71	19.53	18.27	21.47	18.73
					0.050	1.08								
53W002b	0.193	W4	0146	0354	17 14 09.564	+50 15 27.22	0.6/0.5	062	0.53/0.27	2.5	20.48	18.78	19.54	17.67
					0.037	0.07								
53W002c	0.273	W3	0167	0176	17 14 08.901	+50 14 40.39	1.0/0.8	040	0.22/0.15	10.0	19.81	18.07	19.03	17.20
					0.029	0.19								
53W002d	0.275	W2	0389	0208	17 14 14.335	+50 14 32.41	1.0/0.9	089	0.45/0.29	5.0	19.63	17.63	19.49	16.75
					0.007	0.57								
53W002e	0.528	W3	0601	0202	17 14 08.268	+50 13 57.00	1.5/0.6	171	0.35/0.18	3.3	20.53	18.43	20.93	18.24
					0.032	0.29								

[a] Galaxy name. 53W044, 53W046, and 53W002 indicate LBDS radio galaxies. The other object names indicate several field galaxies also detected in the WFC frames.

[b] CCD number of the WFC I-band detection.

[c] (X, Y) pixel coordinates of the galaxy core in this CCD.

[d] Right ascension and declination (equinox J2000) of the galaxy core, averaged over the astrometry in the WFC frames and in the ground-based CCD images. The second line gives the observed rms error over all available astrometric measurements.

[e] De Vaucouleurs half-light radius r_e and exponential scale length r_s, respectively, of the *simulataneous* best model-fit bulge + disk to the *raw* WFC image. If no value for the disk is quoted in cols. (8) and (10), a meaningful disk could not be fit to the raw data.

[f] Average sky position angle (measured from north through east) of the outer semimajor axis of this best model fit, corrected for the *HST* spacecraft orientation. The real best-fit sky position angle and ellipticity vary with radius (see also Figs. 2–4).

[g] Average best model-fit ellipticity of the inner bulge and outer disk, respectively.

[h] Bulge-to-disk ratio of the best model fit to the *raw* I-band image (which usually has the best S/N).

[i] Integrated V and I magnitudes of the best model fit to the *raw* images, using the WFC zero points discussed in the text.

[j] Average central surface brightness (within 0″.1 radius) of the best model fit to the *raw* V- and I-band images.

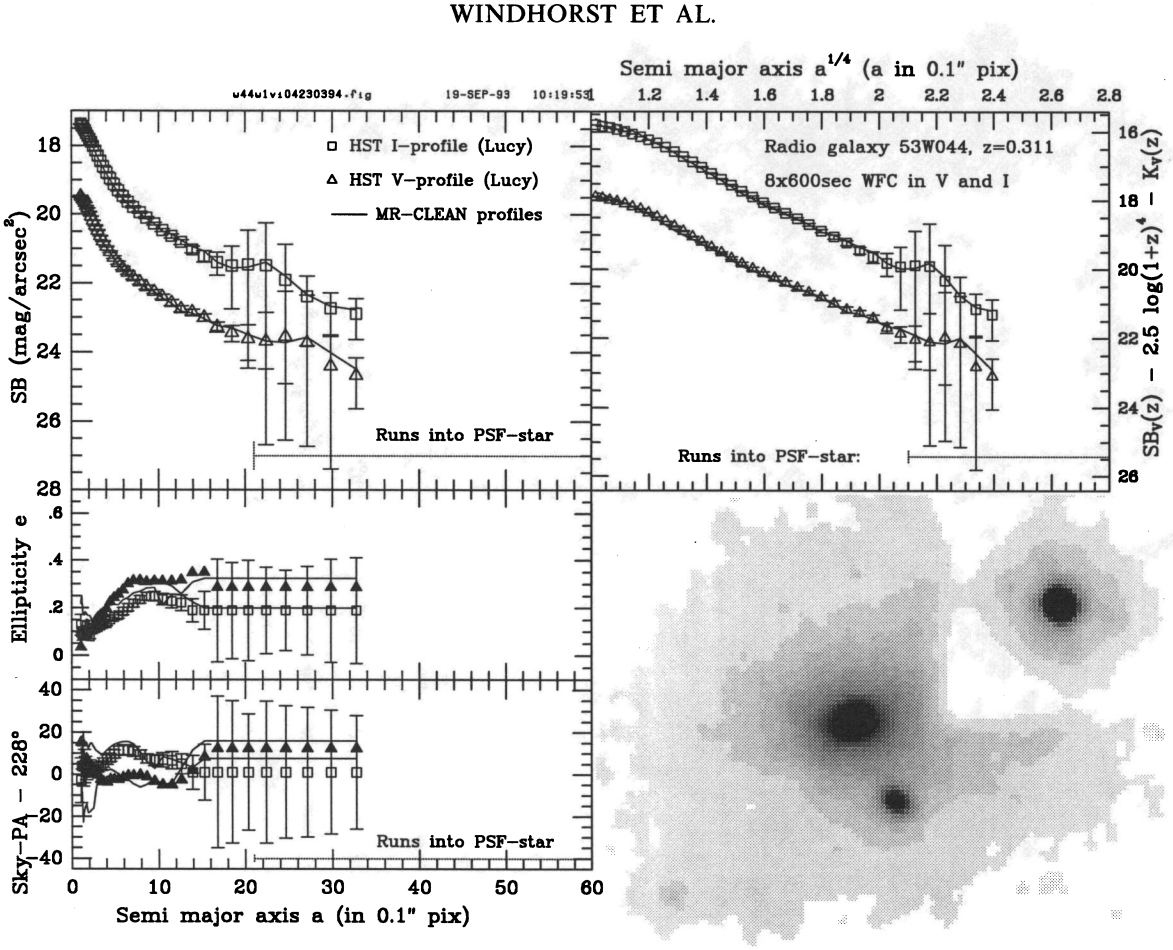

FIG. 2a

FIG. 2.—(*a*) Isophotal profiles SB(V) and SB(I), ellipticity (e) and position angle (P.A.) vs. a (*left panels*) and vs. $a^{1/4}$ (*right panel*) for the early-type (S0) radio galaxy 53W044 at $z = 0.311$. Open squares indicate Lucy-ed I-band images, while open or filled (for clarity) triangles indicate Lucy-ed V-band images. Solid lines indicate the MR-CLEANed data. The lower right panel in each of Figs. 2–4 displays a gray scale of the Lucy-ed image—usually in I—that covers about 10″.9 × 8″.8. The position angles are measured counterclockwise with respect to the positive Y-axis of the appropriate CCD, and converted to true sky position angles by subtracting the *HST* spacecraft orientation angle (displayed along the Y-axis of the lower left panel). The upper right axis displays the V-band SB scale K-corrected to zero redshift, using the models of § 5. The positive Y-axis of this gray-scale image points to the right. An empty box is created around the deconvolved PSF star 5″.5 away from 53W044, which has been convolved back to 0″.2 FWHM to get proper sampling. (*b*) As in (*a*), but for the early-type galaxy 53W046 at $z = 0.528$. The positive Y-axis of the gray-scale image points to the right. Note the $a^{1/4}$ law in both V and I. (*c*) As in (*a*) but for the elliptical field galaxy 53W002a at $z = 0.58$. The positive Y-axis of the gray scale image points upward. While all other gray-scale images show Lucy deconvolutions, this is the only figure which displays the MR-CLEANed image, which should be compared to the Lucy-ed image of the *same* area in Fig. 3*a*. 53W002a is the brighter object in the center.

(§ 2.2), and the error in the sky subtraction (§ 2.2). We estimate that the PSFs for the radio galaxies (measured at the same CCD location to within 5–50 pixels) yield deconvolutions of at most 20–25 dB dynamic range (5–6 mag), and about 16 dB (4 mag) for the field galaxies whose PSF was typically 50–100 pixels away. The algorithm provides formal fitting errors, but since the *HST* images suffer from spherical aberration and have been deconvolved, the isophotal data points are *not* independent, as discussed by W94c.

3.3. *Reliability of the Deconvolutions*

We used the same approach as W92 and KW93 to construct an array of isophotal models, convolved these with the PSF, and fit these to the *raw HST* images of all objects, yielding optimized estimates for r_e or r_s, central SB, e, and P.A. We find that the optimal model-fit parameter values are within their formal errors consistent with the values derived from isophotal fits to the deconvolved images (see §§ 4–6 and Table 3).

The reliability of the deconvolved images can be assessed from the consistency between the two (nearly) photon-preserving deconvolution algorithms: Lucy and MR-CLEAN. Sections 4–6 show that both algorithms yield globally consistent images and light profiles (within the statistical and external errors of the data) over a large enough range in a that these galaxies can be classified. We emphasize that *no* deconvolution algorithm known to us (neither in radio nor in optical) produces unique solutions. Yet, the Lucy and MR-CLEAN methods produce statistically consistent light profiles in §§ 4–6.

4. RESULTS FOR COMPACT RADIO AND FIELD GALAXIES AT $z = 0.3$–0.6

In this section, we give individual discussions of the two high-SB radio galaxies with $z = 0.311$ and 0.528 and the compact field galaxy at $z = 0.58$. KW93 display the deconvolved WFC images of 53W044. In § 5, we discuss the young compact radio galaxy at $z = 2.390$ in more detail than presented in W92. The current paper displays new images for 53W046 and *all* the field galaxies with MMT redshifts, and presents the

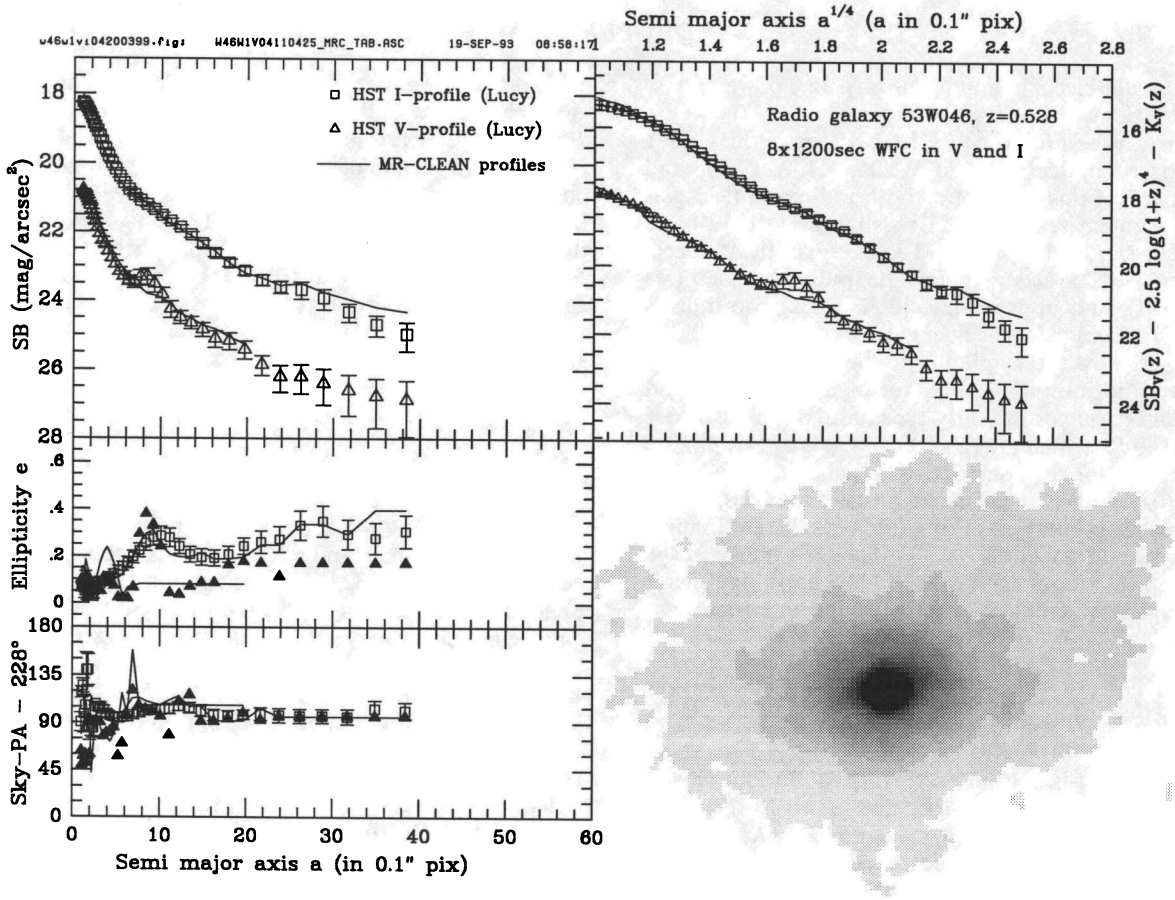

FIG. 2*b*

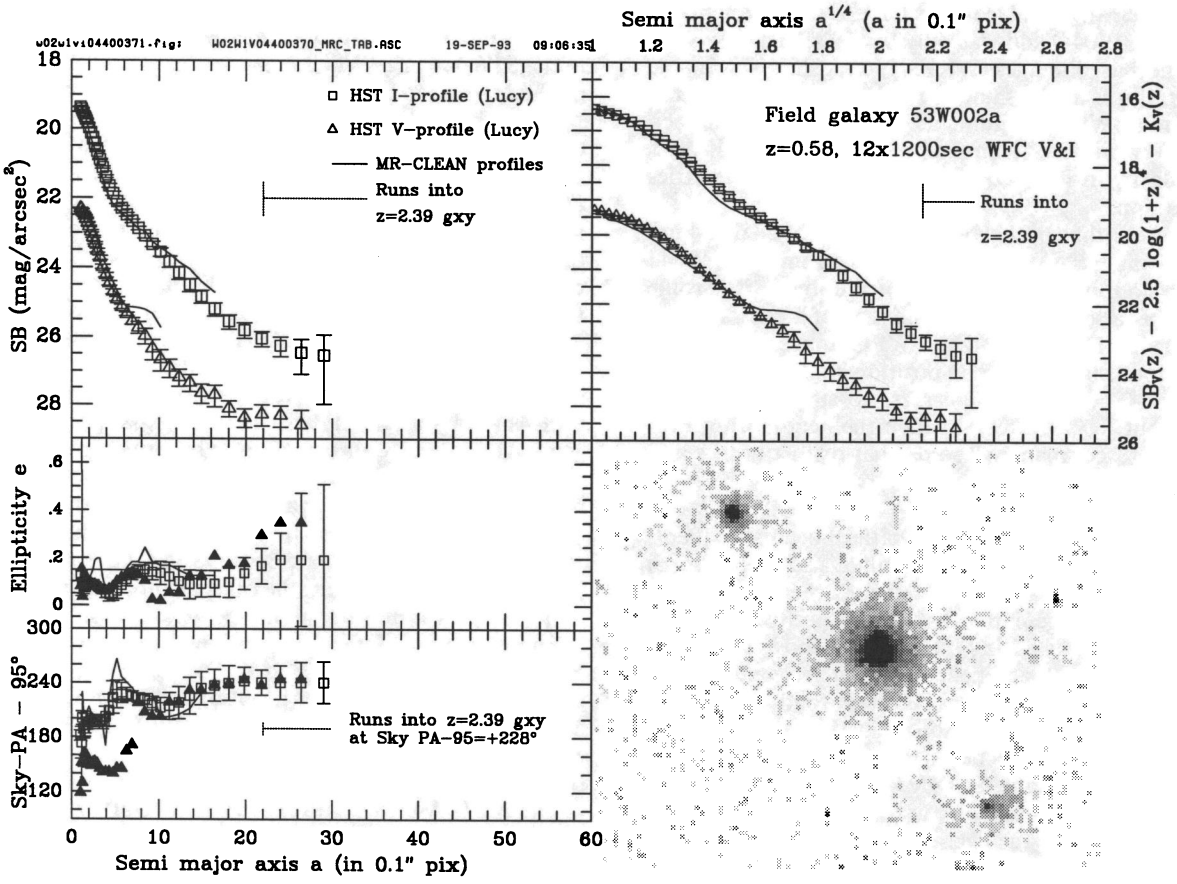

FIG. 2*c*

light profiles of *all* objects in a uniform way. In § 6, we discuss the six field galaxies with $z = 0.1$–0.6.

Radio maps can be found in WHK and Oort et al. (1987), and ground-based optical data in WKK, KKW, W91, and § 2.8 and Table 2 of this paper. For both radio and field galaxies, Table 2 summarizes the MMT redshifts and the 12-band m_{2750} *UBVRIgriJHK* photometry. Table 3 gives (R.A., Decl.) coordinates of $\sim 0\farcs25$ accuracy for the radio galaxies (see WKK and W91), and approximate (R.A. Decl.) coordinates with $\sim 0\farcs3$–$0\farcs5$ accuracy for the field galaxies.

Figures 2*a*–2*c* show the isophotal profiles SB(V) and SB(I), ellipticity e, and position angle P.A. versus a (*left panels*) and versus $a^{1/4}$ (*right panel*) for the early-type radio or field galaxies with $z = 0.311$–0.58, which are (giant) ellipticals or S0s. Figure 3*a* shows the same for the compact radio galaxy at $z = 2.390$. Figures 4*a*–4*f* show the same for the six field galaxies, which are (early-type) disk galaxies at $z = 0.131$–0.528. In Figures 2–4, each lower right panel displays a gray-scale image of the deconvolved object (about $10\farcs9 \times 8\farcs2$ in all cases), in either I or V depending on which filter has most visible or structure at high S/N.

4.1. *Radio Galaxy 53W044 at z = 0.311*

The object 53W044 is a $V = 19.4$ mag LBDS radio galaxy with $S_{1.4} = 1.75$ mJy and $\alpha_{1.4}^{0.6} = 0.92$ (W84). Its MMT spectrum shows no emission lines, but a clear H and K break at $z = 0.311$ (Fig. 1). The galaxy has central peak S/N of about 60 before deconvolution and is at least 45 pixels across in WF1.

The raw and deconvolved images show that 53W044 also has a faint extended "companion" with $V \simeq 23.4$ mag. This "companion" is clearly resolved in its CLEAN components (in the direction of 53W044) and was only barely seen as a wisp in our best ground-based images (WKK). No redshift is available for this object. If it is at the same redshift, it would be about 5 kpc away from 53W044. Arguments for the physical association of 53W044 and its "companion" are given by KW93, based on similarity in $V-I$ colors, and low-level asymmetries in the "companion."

Figure 2*a* shows that both V and I profiles of 53W044 are consistent with an $a^{1/4}$ law. Since the spectrum of 53W044 shows no emission lines, any AGN contribution to its profile must be small, as also suggested by the lack of a central point source in both the FOC/48 and the WFC images. Figure 2*a* shows its isophotal ellipticity e and position angle P.A. versus a on scales of $0\farcs2$–$2\farcs5$. Within the errors, no significant distortions are seen out to $2\farcs0$, beyond which the neighboring PSF star and the faint "companion" somewhat distort both e and P.A.

53W044's ellipticity increases from $e = 0$ at $a = 0$ to a stable value $e \sim 0.25 \pm 0.05$ at $a \gtrsim 0\farcs8$. This pattern occurs frequently for galaxies dominated by an inner bulge and an (inclined) outer disk (see also §§ 6.1–6.6) and indicates the transition of the rounder bulge into the flatter disk. The other two compact early-type galaxies discussed in §§ 4.2 and 4.3 show a different behavior. They show no significant trend in e versus a. We therefore believe that 53W044 is an S0 rather than an elliptical galaxy at $z = 0.311$. This conclusion is further supported by the detailed model fitting to the aberrated image by KW93, who iteratively fit a simultaneous bulge plus disk contribution, and find evidence for a modest color gradient.

In the LBDS, 53W044 was classified as an elliptical galaxy with radio power $\log P_{1.4} = 23.98$ W Hz^{-1}. This is about 1.0 dex below the FR-I–FR-II break, which occurs at $\log P^* \simeq 25.0$ W Hz^{-1}, and is also typical for an S0 galaxy. The VLA A-array map of 53W044 (Oort 1987) shows a rather compact structure with largest angular size LAS $= 1\farcs9 \pm 0\farcs2$ like those of FR-I radio galaxies. These two radio properties, its *HST* light profile, and its e versus a behavior suggest that 53W044 is an S0 galaxy at $z = 0.311$. Weak radio galaxies with early-type spectra are thus not necessarily always (giant) elliptical galaxies, but could be S0s, whose ground-based long-slit spectrum will be dominated by the old stellar population in its central bulge.

4.2. *Radio Galaxy 53W046 at z = 0.528*

The object 53W046 is a $V = 21.1$ mag LBDS radio galaxy with $S_{1.4} = 63.1$ mJy and $\alpha_{1.4}^{0.6} = 0.69$. Its spectrum shows only very weak O [II] $\lambda 3727$ in emission, and has a clear H and K break at $z = 0.528$ (Fig. 1). In the LBDS, it was classified as a giant elliptical galaxy with radio power $\log P_{1.4} = 26.02$ W Hz^{-1}, about 1.0 dex above the FR-I–FR-II break. The galaxy has central peak S/N of about 30, and is at least 35 pixels across in WF1. Figure 2*b* shows that both the V and I profiles of 53W046 are consistent with a de Vaucouleurs profile. Note that a few Lucy and MR-CLEAN points are marginally inconsistent (within the errors) for $a \simeq 8$ pixels. Except for the divergence of MR-CLEAN at low SB levels (for $V \gtrsim 25.5$–27 mag arcsec^{-2} and $I \gtrsim 24$–25 mag arcsec^{-2} in all figures) and the use of an imperfect PSF in the case of 53W044b in one chip corner (§ 6.6 and Fig. 4*f*), this is the only case where Lucy and MR-CLEAN produced a few inconsistent points. The reason for this is possibly a few hot pixels left in the 53W046 images, which were not seen in our time-dependent hot-pixel maps or in the 53W044 or 53W002 images. The MR-CLEAN and Lucy methods respond to remaining hot pixels differently.

Since the spectrum of 53W046 shows no strong emission lines, any AGN contribution to its light profile must be small. Its WFC light profiles and its rather large optical flux (Table 2) at this redshift (KKW) suggest that 53W046 is a giant elliptical galaxy at $z = 0.528$. Figure 2*b* shows its isophotal ellipticity and position angle. Within the errors, no significant isophote distortions are seen out to $2\farcs5$. The plotted values for the V band are uncertain because 53W046 is fainter and more irregular in V. Most of this "irregular" flux was visible at the 5–10 σ level in the undeconvolved image. After all CRs were removed down to the 2 σ level, we took great care to make sure that CLEAN did not amplify any hot pixels that persisted with the same ADU flux in all exposures. Only one obvious hot pixel was found and removed. 53W046's deconvolved morphology in the V band resembles that of 3C 305 at $z = 0.041$ (Heckman et al. 1982), an object of somewhat more irregular morphology. Its I profile is more regular. Because its 4000 Å break is shifted just past the F555W filter, the object is much fainter in V than in I, so we cannot say if the V image indicates a merger remnant. Much of the lumpy structure in the V image of 53W046 is not seen in I, and the de Vaucouleurs profile is a good fit in both V and I. At the suggestion of D. Burstein, we also fitted a bulge + disk to the 53W046 image, but found $B/D > 10$ and could not find a good fit for a pure disk without bulge (see Table 3).

The VLA A-array map of 53W046 (Oort et al. 1987) also shows a somewhat irregular radio structure. It has LAS $= 3\farcs2$

$\pm$ 0".3, and resembles an FR-I radio galaxy with a poorly resolved jet, surrounded by a low-SB halo. The radio power of the FR-I–FR-II break itself may increase with redshift due to the cosmological evolution of the radio source population, if the latter manifests itself as luminosity evolution (W90). If the P^* value increases as $(1+z)^{+5}$ (e.g., W90), the radio luminosity of 53W046 at $z = 0.528$ would be less than the P^*-value expected at that redshift, explaining why the object has a radio morphology similar to an FR-I source. The optical kiloparsec-scale axes of both 53W044 and W046 are not obviously aligned with the VLA radio axis of Oort et al. (1987). This is not surprising, since both galaxies may have FR-I radio morphology and are expected to be dynamically relaxed at $z = 0.3$–0.5. Hence, traces of any alignment effect in weak radio galaxies at higher redshift (see W91) would have disappeared.

4.3. *Field Elliptical 53W002a at z = 0.58*

Objects 4 and 5 in the 200 inch Four-Shooter images of W91 are clearly faint field galaxies in our *HST* WFC images (which are reproduced in Fig. 1 of W92). The compact Object 6 of W91 has $V \sim 22.9$ mag and is very red in $V-I$. In our *HST* images, we refer to their Object 6 as "53W002a." It was classified as a star by W91. Figure 2*c* clealy shows that this object (the brightest one near 53W002 in Fig. 2*c*) is actually a very compact galaxy with a measured light profile close to an $a^{1/4}$ law. Exponential laws do not provide good fits to the data over a large range in a. Note that for $a \gtrsim 2''.2$, 53W002a's light profile runs into that of the $z = 2.390$ galaxy 53W002 (see Fig. 2*c*).

53W002a is our only galaxy for which the MMT redshift is not yet secure. The red WFC $V-I$ and ground-based colors of 53W002a suggest that its H and K break is redshifted past the middle of the V band, so that its redshift must be at least $z \gtrsim 0.4$. Since the object is still rather bright in the I-band image (reproduced in Fig. 2 of W92), its redshift must also be $z \lesssim 1.05$. A recent 2 hr MMT spectrum shows a possible H and K break and G band at $z = 0.58 \pm 0.005$ (Fig. 1). In this and other MMT spectra, the sky subtraction is corrupted around the 6300 Å line, so we cannot yet confirm this redshift. However, in all our independent MMT spectra, 53W002a's continuum flux is definitely suppressed below 6180 Å and takes off past 6350 Å, so its redshift is most likely in the range $0.56 \lesssim z \lesssim 0.60$. No obvious other breaks were seen at longer wavelengths in low-S/N MMT spectra out to 8500 Å, which would place its only alternative redshift at $z \gtrsim 1.0$. We consider this unlikely given its observed high SB and its apparent magitudes (see Tables 2 and 3). Since the *UBgri* (W91) and U^+ J^+ *FN* colors (KKW) of 53W002a are also consistent with $z = 0.58 \pm 0.01$, we will consider this to be its correct redshift, unless better spectra point to the contrary. Given its $a^{1/4}$-like light profile, 53W002a is probably an elliptical field galaxy at $z = 0.58$. The object is overall ~ 1.7 mag fainter than the gE radio galaxy 53W046 at nearly the same redshift and is thus likely an ordinary field elliptical at $z = 0.58$.

It is thus not surprising that W91 misclassified their Object 6 as a star, since distant gE galaxies may show up as stellar objects in average ground-based seeing (Kristian 1973). W91 used the $V-K$ colors of this object to check the calibration and large-scale gradient removal of their K-band image. Since their Palomar K-band images were photometric—they yield K-band magnitudes consistent with our UKIRT images—their misclassification of 53W002a as a star is of no further consequence to their K-band photometry.

5. RESULTS FOR THE COMPACT RADIO GALAXY AT $z = 2.390$

5.1. *Clues to 53W002 from HST and Ground-based Data*

The first results from the 12 WFC exposures in V and I on the weak high-redshift ($z = 2.390$) radio galaxy 53W002 were discussed and displayed by W92. In § 5.2, we use limits to 53W002's *HST* color gradients to constrain its possible age gradients. In this section, we first briefly summarize the main characteristics of 53W002, needed to follow the discussion in § 5.2:

1. At $z = 2.390$, 53W002's radio power ($\log P_{1.4} = 27.73$ W Hz^{-1}) is ~ 2.7 dex larger than the P^*-value that separates FR-II from FR-I sources at $z = 0$ (W90, W91), and $\gtrsim 5$ dex larger than the most powerful known radio spirals at $z = 0$, so that 53W002 likely belongs to the parent population of early-type galaxies, and thus is not likely to have had a disk at $z = 2.390$.

2. 53W002 is clearly resolved in an unresolved central source (AGN) and an extended galaxy envelope (Fig. 3*a*). Its unresolved core contributes at most 20% in V ($\lambda_{\rm rest} \simeq 1600$ Å) and 25% in I ($\lambda_{\rm rest} \simeq 2600$ Å; W92), consistent with ground-based spectroscopy, which limits the AGN contribution to 53W002's continuum to $\lesssim 35\% \pm 15\%$ (W91). Most of the galaxy's light comes from the central 1".1 radius, or $\simeq 8$ kpc.

3. Elliptical isophote fits to the WFC images only show a marginal elongation (with $e = 0.15 \pm 0.10$) of the V- and I-band continuum at sky P.A. $\simeq 105° \pm 15°$ (Fig. 3*a*), although the outermost isophotes are most elongated. At 0".2 FWHM resolution, the *HST* continuum of 53W002 thus has—within the errors—the same sky position angle as the (marginally resolved) ground-based continuum (P.A. $= 101° \pm 14°$) and the redshifted Lyα (P.A. $= 96° \pm 5°$) and VLA 8.4 GHz (P.A. $= 90° \pm 3°$) images of W91. However, the physical size ($\lesssim 0''.6$, or ~ 8 kpc at $z = 2.390$) of any continuum "alignment effect" in this lower power radio galaxy is small compared to that in the most luminous high-redshift radio galaxies.

4. Figure 3*a* and Table 3 show that 53W002 has a radial intensity profile that can be fitted by a de Vaucouleurs profile in I, using the modeling method described in W92 and KW93. In V, 53W002's profile is steeper, but—within the errors—almost straight in $a^{1/4}$. That is, 53W002 has a "generic" galaxy profile at $z = 2.390$, in contrast with the much larger, clumpy ultraluminous radio galaxies observed from the ground (e.g., McCarthy et al. 1987; Chambers et al. 1990; Miley et al. 1992). Note that for $a \gtrsim 1''.2$, 53W002's light profile starts to overlap with that of the field elliptical 53W002a at $z \simeq 0.58$ (Fig. 2*c*).

The PSF-modeling method yields a point-source contribution of $30\% \pm 10\%$ and an effective radius $r_e \simeq 10$–12 pixels (along the major axis). This corresponds to $r_e = 13$–16 kpc for the largest universe ($H_0 = 50$ and $q_0 = 0$) and to $r_e = 4$–5 kpc for the smallest one ($H_0 = 100$ and $q_0 = 0.5$). Note that for $H_0 = 75$ and $q_0 = 0.1$, we get $r_e = 8.3$ kpc, remarkably close to the 8.2 kpc given by the RC2 for nearby luminous early-type galaxies, such as M87 (de Vaucouleurs, de Vaucouleurs, & Corwin 1976; see also W92). If 53W002 were to evolve into an early-type galaxy and *if* the effective radius of such galaxies has not appreciably evolved since $z \simeq 2.5$ (nondissipative evolution of today's nondissipative systems), then the scale length from our χ^2 fitting is more consistent with the RC2-values if $H_0 \simeq 75$ km s^{-1} Mpc^{-1}.

Similar model fits are discussed for the other galaxies in our Cycle 1 *HST* images in § 6.

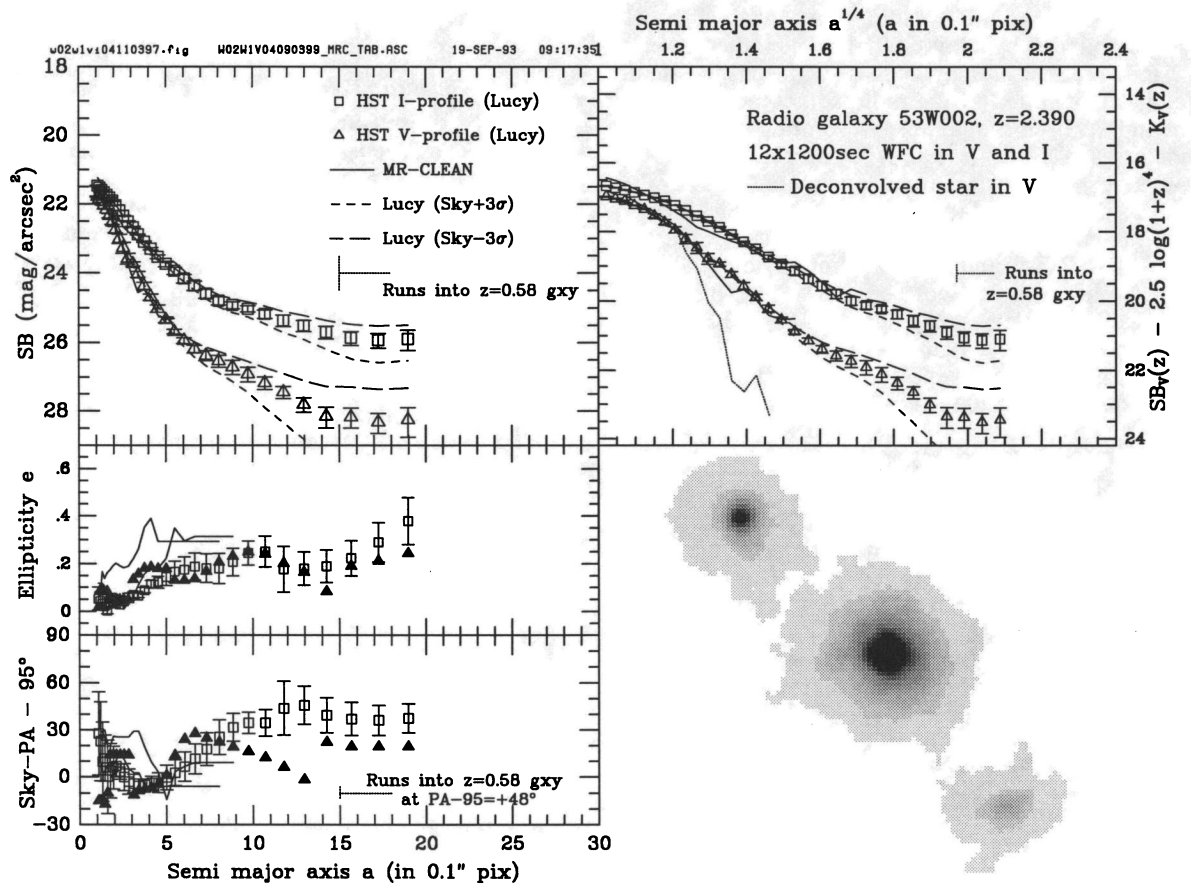

FIG. 3a

FIG. 3.—As in Fig. 2*a*, but for the compact radio galaxy 53W002 at $z = 2.390$. The positive Y-axis of the gray-scale image points upward. 53W002 is the fainter object to the upper left. The dotted line in the upper right-hand panel is a deconvolved star (*not* the PSF; see Fig. 3 of W92), and indicates 53W002's AGN contribution in V. For radii $a^{1/4} \lesssim 1.3$ ($a \lesssim 0\farcs3$), 53W002 shows excess light from the central point source that contains about 30% ± 10% of the total light. The dashed lines indicate $\pm 3\,\sigma$ errors in sky subtraction. For $a^{1/4} \gtrsim 1.4$ ($a \gtrsim 0\farcs4$), 53W002's profile is consistent with an $a^{1/4}$ law. The radio galaxy shows marginal color gradients in $V-I$ rising from ~ 0.3 mag at $a \sim 0\farcs2$ to ~ 1.2 at $a \gtrsim 0\farcs4$, and to ~ 2.2 at $a \sim 1\farcs2$. (*b*) Light profiles for the three compact LBDS radio galaxies ($z = 0.311$–2.390) as well as the compact field galaxy at $z = 0.58$ in the *HST* V and I bands, as well as the UKIRT K-band images. The *HST* profiles were deconvolved, and convolved back to the UKIRT $\sim 1\farcs0$ FWHM resolution to see if significant optical-IR color gradients are present at large radii. None are visible for the three galaxies with $z \lesssim 0.6$. (*c*) $J^+ - N$ ($\simeq V - I + 0.30$ mag) color-redshift diagram for the combined LBDS radio galaxy sample with spectroscopic redshifts. Filled symbols are extended radio sources (LAS $\gtrsim 1\farcs4$). Open symbols are unresolved radio sources at the $1\farcs4$ FWHM VLA resolution. Circles are high-SB galaxies (usualy red gEs and extended radio sources). Triangles are low-SB galaxies (usually bluer colors and unresolved radio sources). Pentagons are quasars, Seyfert galaxies, or LINERs. Predictions are from Bruzual's spectra evolution C-models (see § 5) with a constant initial starburst of 1 Gyr duration, plotted at *current* ages of 5–16 Gyr for 1 Gyr increments, corresponding to $z_{form} \simeq 0.4$–6 (for $H_0 = 50$ and $q_0 = 0.1$). The allowable range of 53W002's color gradient is indicated by the vertical dotted line at $z = 2.390$, which limits its stellar population age gradient to ~ 0.3–1.0 Gyr. The C-models with ages 13, 14, and 15 Gyr have $z_{form} = 2.4$, 3.4, and 5.3, respectively. They brace our *HST* + UKIRT limits to 53W002's color gradients, and constrain its initial starburst epoch to $z_{form} \simeq 2.5$–4 (~ 13.5–14.2 Gyr), (*d*) $I-K$ color-redshift diagram of the combined LBDS radio galaxy sample with spectroscopic redshifts. Symbols and models are as in (*c*). The lack of significant color gradients in $I-K$ is indicated by the vertical dotted line at $z = 2.390$, which limits the stellar population age gradient to $\lesssim 0.5$–1.0 Gyr.

5.2. *Limits to 53W002's Color Gradients*

Figure 3*a* suggests that the color profile of 53W002 is rather flat at $V-I \simeq 0.34 \pm 0.20$ mag in the inner part ($a \sim 0\farcs2$), which is affected by its weak AGN (see dotted line in upper right panel of Fig. 3*a*). A $V-I$ color of ~ 0.3 mag is also expected for a young actively star-forming galaxy at $z = 2.390$ (see lower left panel of Fig. 3*b*), illustrating that young galaxies can have colors indistinguishable from AGNs. Bearing in mind the uncertainties introduced by Lucy and MR-CLEAN at low SB levels (§§ 2 and 3), Figure 3*a* suggests that 53W002's profile may redden to $V-I \simeq 1.2 \pm 0.3$ mag at $a \gtrsim 0\farcs4$, and to possibly $V-I \gtrsim 2.2 \pm 0.3$ mag for at $a \gtrsim 1\farcs2$. The long- and short-dashed lines in Figure 3*a* show the effect of formal $\pm 3\,\sigma$ errors in the sky subtraction. Given that (1) such errors in the sky subtraction are possible (§ 2.2), (2) 53W002's light profile overlaps with that of the very red $z \simeq 0.58$ field galaxy 53W002a for $a \gtrsim 1\farcs2$ (Figs. 2*c* and 3*a*), and (3) 53W002's Lucy and MR-CLEAN V-band deconvolutions start to disagree for $a \gtrsim 0\farcs5$ (or $V \gtrsim 25.5$ mag arcsec^{-2}), we cannot say with certainty that 53W002's $V-I$ color reddens to more than ~ 1.5 mag at $a \gtrsim 1\farcs0$, and we consider its likely reddest color to be $V-I \simeq 1.2 \pm 0.3$ mag at $a \gtrsim 1\farcs0$. At the flux-weighted average radius $a \simeq 0\farcs5$, 53W002's color is also $V-I \sim 1.2 \pm 0.2$ mag, similar to the ground-based colors in the best seeing images of W91 (all available photometry is summarized in our Table 2).

To interpret possible (limits to) color gradients of 53W002,

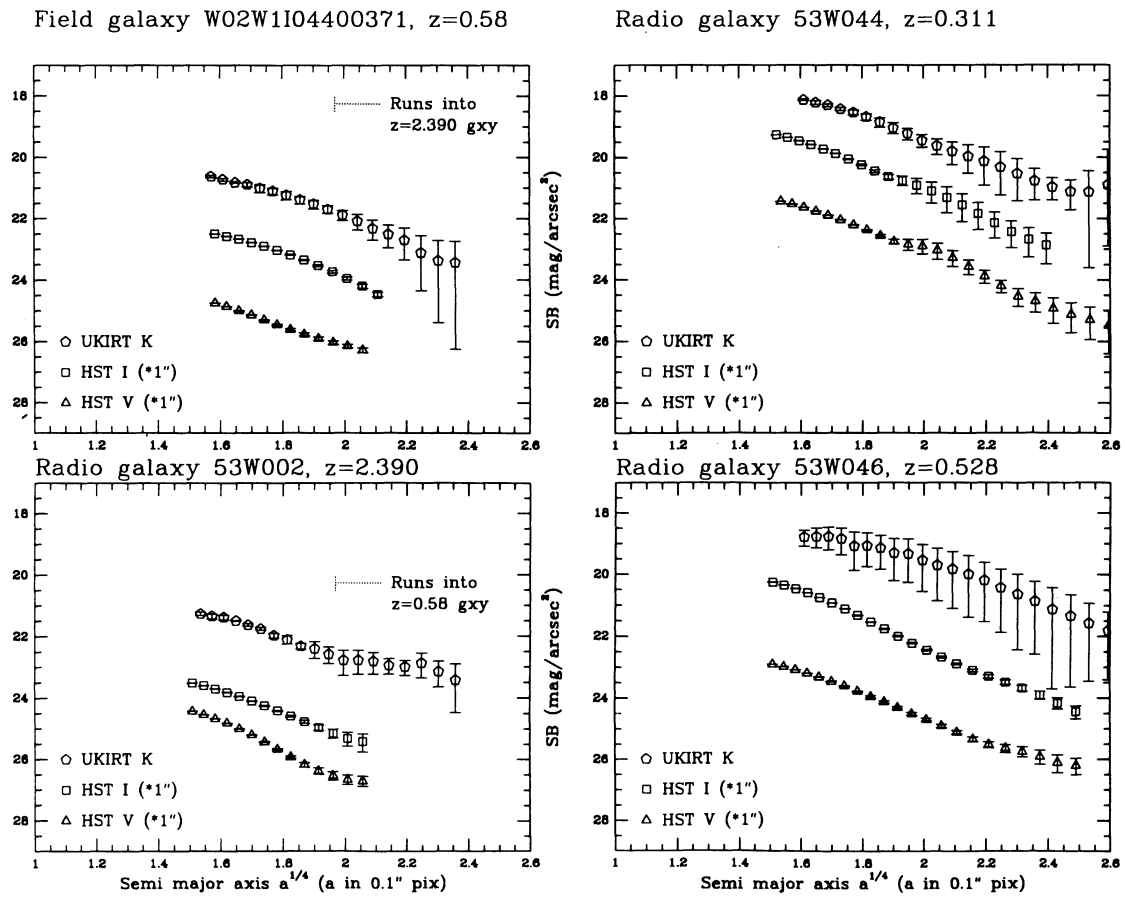

FIG. 3*b*

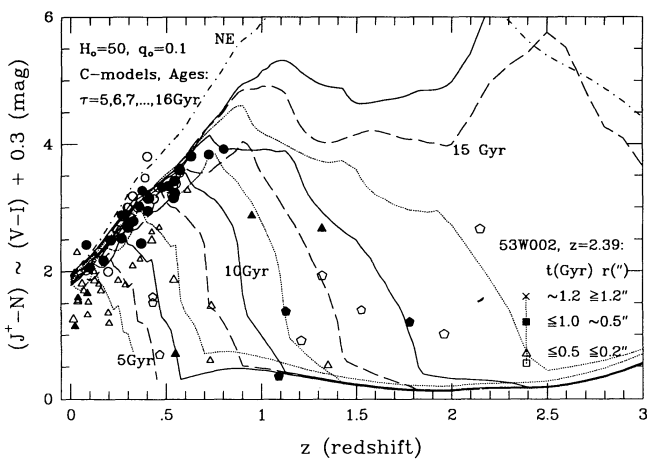

FIG. 3*c*

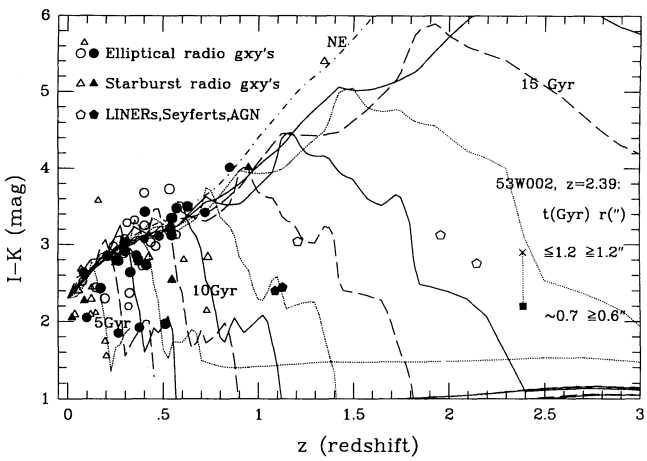

FIG. 3*d*

we need to compare these observed $V-I$ colors to spectral evolution model predictions at that redshift for various possible star formation histories and galaxy ages (or formation redshifts z_{form}, assuming a world model). Therefore, Figure 3*c* shows the $J^+ - N$ color-redshift diagram of the combined LBDS radio galaxy sample with available spectroscopic redshifts (WKK; KKW; W85; W90). This is the closest LBDS filter system to *HST*'s $V-I$ color for which we have multicolor photometry and spectroscopic redshifts from many radio galaxies. An approximate transformation yields: $(J^+ - N) \simeq (V-I) + 0.30$ mag (see W91). Filled symbols in Figures 3*c* and 3*d* indicate extended radio sources (LAS $\gtrsim 1''.4$), open symbols indicate 1.4 GHz radio souces that are unresolved at the $1''.4$ FWHM VLA A-array resolution. Circles are high-SB radio galaxies (KKW) with upper envelope colors, which are likely giant ellipticals (as confirmed by their large absolute lumi-

nosities; KKW; W90), and are usually extended radio sources (see also KKW). Triangles are low-SB radio galaxies, which have in general bluer colors and are usually unresolved sources (see also Oort et al. 1987). Pentagons are quasars (at $z \gtrsim 1$), or Seyfert galaxies and LINERs (at $z \lesssim 1.0$).

In Figures 3*c* and 3*d*, we show predictions from the spectral evolution "C-model" of Bruzual (1983, 1988), which has an initial burst of constant star formation (and zero thereafter) of 1 Gyr duration. The C-models were computed for current galaxy ages of 5–16 Gyr with 1 Gyr increments, corresponding to a wide range of formation epochs in the range $z_{\rm form} \simeq 0.4$–6 (for $H_0 = 50$ and $q_0 = 0.1$). These single-burst models are not unique, but do describe all the weak radio galaxy color-redshift data quite well. The C-models with current ages 13, 14, and 15 Gyr have $z_{\rm form} = 2.4$, 3.4, and 5.3, respectively. They brace the constraints from our *HST* + UKIRT limits to 53W002's color gradients and limit its initial starburst epoch to the rather narrow range of $z_{\rm form} \simeq 2.5$–4 (current ages $\simeq 13.5$–14.2 Gyr), as shown in Figures 3*c* and 3*d*.

To derive the *K*-corrected SB scale displayed on the right axis of *all* right-hand panels in Figures 2–4, we used similar Bruzual models. Using the resulting differential *K* corrections, we transformed 53W002's apparent $V-I$ color gradient to $J^+ - N$, and plotted its $J^+ - N$ colors in Figure 3*c* at the three radii quoted above ($a = 0\farcs2$, $0\farcs5$, and $1\farcs2$) connected with a vertical dotted line at $z = 2.390$. The apparent color gradient in 53W002 corresponds to a color of $J^+ - N \sim 0.7$ at $a \lesssim 0\farcs2$ that increases to $J^+ - N \sim 1.6$ at $a \gtrsim 1\farcs0$. The corresponding stellar population ages at $z = 2.390$ are $\lesssim 0.2$–0.5 Gyr (main-sequence [MS] turn-off at B9 V–A2 V) for $a \lesssim 0\farcs2$ ($\lesssim 1.5$ kpc) to ~ 1.2 Gyr (MS turn-off at A4 V–A6 V) for $a \gtrsim 1\farcs0$ (or $\gtrsim 7.5$ kpc). The spectrophotometry and 9-band (Lyα *UBgriJHK*) photometry of W91 showed that 53W002's total spectral energy distribution (SED) suffers little from internal reddening, and that its observed stellar population is dominated by stars of ages $\lesssim 0.2$–0.3 Gyr. The ground-based spectroscopy was thus dominated by the inner $0\farcs2$–$0\farcs4$, or 1.5–3 kpc, which contains most of the light. Any redder outer envelope was not seen in the ground-based spectra, although there was some hint for it in the *K*-band images, which have only marginally converging light profiles (see W91). Our UKIRT *K*-band image has better seeing and shows a marginal faint red outer envelope (see Fig. 3*b*, which still has large errors).

To illustrate this further, we show the UKIRT *K*-band profiles of 53W044 at $z = 0.311$, 53W046 at $z = 0.528$, 53W002a at $z = 0.58$, and 53W002 at $z = 2.390$ in Figure 3*b*, together with their *HST* *V* and *I* profiles. For this, the latter had to be convolved to $1\farcs0$ FWHM to allow for proper inspection of any $V-K$ and $I-K$ color gradients at the coarsest available (UKIRT) resolution. With the poor sampling of the UKIRT images, most *K*-band profiles are consistent with $a^{1/4}$ laws, with little or no evidence for $V-K$ or $I-K$ color gradients in the three lower redshift galaxies ($0.3 \lesssim z \lesssim 0.6$). The $I-K$ color of 53W002 is also fairly constant at $I-K \simeq 2.5 \pm 0.3$ mag from the galaxy core ($\simeq 1\farcs0$) to its outskirts ($a \simeq 2\farcs0$). 53W002 thus shows no evidence for a color gradient in $I-K$ at $1\farcs0$ FWHM resolution. The ground-based UKIRT images provide little information about the $I-K$ color for $a \lesssim 1\farcs0$, and one needs *HST* equipped with the Near-IR Camera and Multiobject Spectrograph (NICMOS) to resolve this situation. Figure 3*d* shows, however, that a constant color of $I-K \simeq 2.5$ mag also constrains the age of 53W002's dominant stellar population at $z = 2.390$ to $\lesssim 1.0$ Gyr in the entire galaxy.

In conclusion, any color gradients in 53W002's $V-I$ light profile vary at most from ~ 0.3 mag at $a \sim 0\farcs2$ to ~ 1.2 mag at $a \gtrsim 0\farcs4$, and to ~ 2.2 mag at $a \gtrsim 1\farcs0$. Together with the rather constant $I-K$ color ($\simeq 2.5$ mag) at $a \gtrsim 1\farcs0$, this is consistent with an aging stellar population that is ~ 0.3–0.5 Gyr old in the galaxy center ($a \lesssim 2$ kpc radius) and possibly ~ 0.5–1.0 Gyr at $a \gtrsim 10$ kpc radius. Let us consider this in comparison with its dynamical appearance. The galaxy 53W002 has undergone sufficient relaxation to have a monotonic *HST* profile without bright clumps. At $z = 2.390$, 53W002 thus already shows the appropriate light profile and scale size consistent with the present-day structure of a luminous high-SB galaxy. Van Albada (1982) has modeled the collapse of both smooth and clumpy protogalaxies, and finds that smooth structure is achieved after a few crossing times (of the final galaxy), or $\lesssim 0.5$ Gyr after turnaround from the Hubble expansion. The physics is similar to that in galaxy mergers, where observations show smooth elliptical-like profiles after a similar time. As argued from its rather large radio power in § 5.1, it is unlikely that 53W002 had a disk at $z = 2.390$. Thus, its collapse must have been rather quick and efficient, otherwise any remaining gas would have likely formed a disk, assuming that a sphere that remains substantially gaseous upon collapse would have left a dominant disk rather than a bulge. Our *HST* images are consistent with 53W002 both starting its dynamical collapse and initial star formation $\lesssim 0.5$–1.0 Gyr before $z = 2.390$. Hence, we believe that 53W002 is also dynamically a young galaxy, although dynamically no younger than its stellar population. Its collapse as protogalaxy likely did not start more than ~ 0.5–1.0 Gyr before $z = 2.390$, or only a few free-fall times, which places its formation redshift at $z_{\rm form} \sim 2.5$–4 (for $H_0 = 50$ and $q_0 = 0.1$), i.e., after the first quasars appeared. This is consistent with the classical galaxy halo collapse model of Eggen, Lynden-Bell, & Sandage (1962), in which the stars in spheroidal components were formed very rapidly, on a time-scale comparable to the collapse timescale of the protogalaxy ($\lesssim 1$ Gyr).

Further constraints to possible color gradients in 53W002 can only come from higher S/N resolution PC imaging without the PSF wings (currently scheduled in an approved Cycle 4 project for 1994 May), and later in the near-IR with NICMOS.

6. RESULTS FOR FIELD GALAXIES WITH EXPONENTIAL DISKS

All objects seen in the deep 200 inch Four-shooter images of W91 are also visible in our *HST* image stack, plus some new ones. Here we discuss the light profiles of six brighter field galaxies with $0.1 \lesssim z \lesssim 0.6$ seen in our WF/PC images. A complete discussion of the Θ-z relation for about 60 *HST* bulges and disks out to $z \simeq 0.8$ is given by Mutz et al. (1994), who also discuss limits to the possible evolution of elliptical galaxy scale lengths.

6.1. *Field Galaxy 53W044a at z = 0.131*

Figure 4*a* shows the field galaxy 53W044a at $z = 0.131$. It clearly has a dominant exponential disk in both *V* and *I* for $a \gtrsim 0\farcs5$ (*upper left panel*), with a small inner $a^{1/4}$-like bulge for $a^{1/4} \lesssim 1.6$ pixels$^{1/4}$ (*upper right panel*). Neither component shows a strong color gradient. At very high contrast, the MR-CLEAN image shows a single set of spiral arms with an inner bar (barely visible in the low-contrast Lucy image of Fig. 4*a*). The sky position angle shows no isophotal twist, and the ellip-

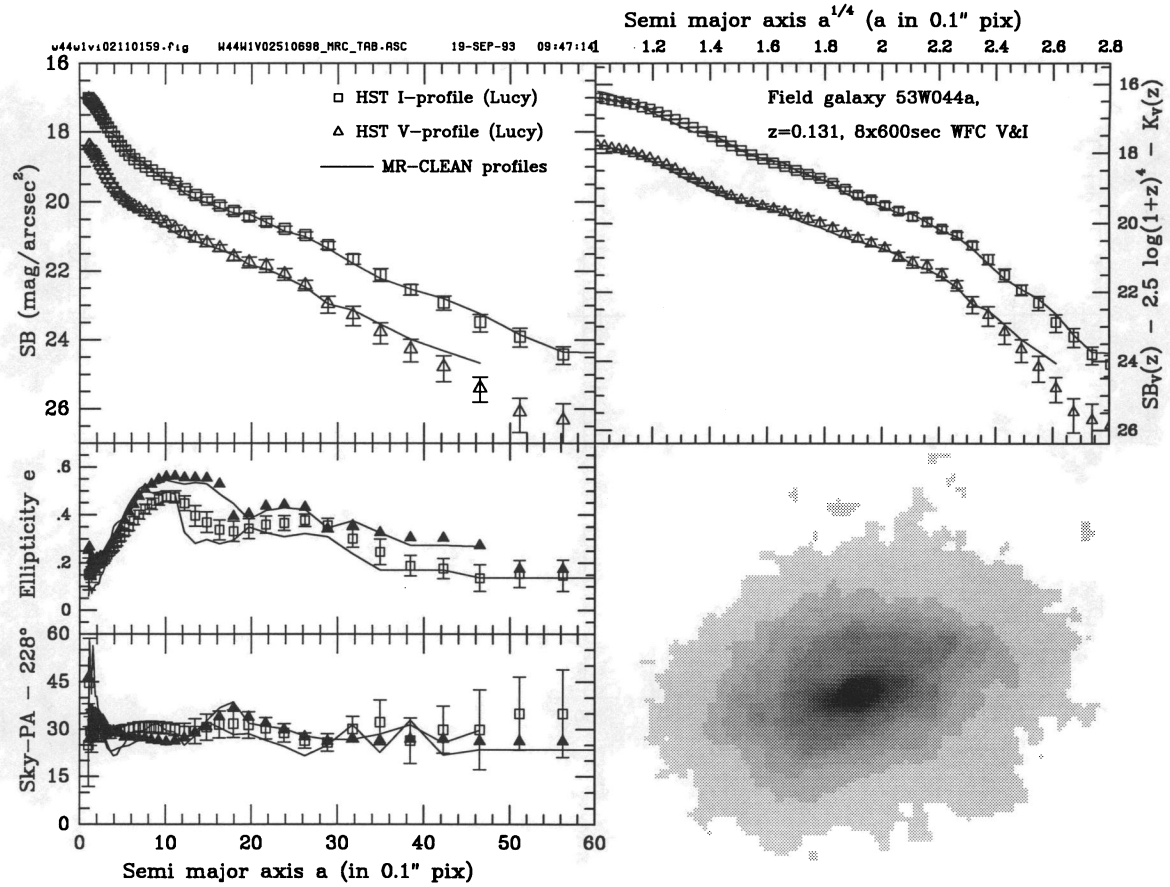

FIG. 4*a*

FIG. 4.—(*a*) As in Fig. 2*a*, but for the barred field spiral galaxy 53W044a at $z = 0.131$. The positive *Y*-axis of the gray-scale image points to the right. At very high contrast, the MR-CLEANed image of 53W044a shows a single set of spiral arms with an inner bar (barely visible in this low-contrast Lucy gray-scale image). Note the large exponential disk in the upper left panel. (*b*) As in Fig. 2*a*, but for the field disk galaxy 53W002c at $z = 0.273$. The positive *Y*-axis of the gray-scale image points upward. (*c*) As in Fig. 2*a*, but for the field disk galaxy 53W002d at $z = 0.275$. The dashed line indicates a MR-CLEANed image that was deliberately done with a PSF that had a few saturated central pixels, which deviates from the proper PSF deconvolution (*solid line*) only by $\lesssim 0.2$ mag in the very core of the *V*-band image. The galaxy has two faint companions with unknown redshifts. The positive *Y*-axis of the gray-scale image points upward. (*d*) As in Fig. 2*a*, but for the field disk galaxy 53W002e at $z = 0.528$. The object has two faint small companions with unknown redshifts, one of which is double. The positive *Y*-axis of the gray-scale image points upward. (*e*) As in Fig. 2*a*, but for the field disk galaxy 53W002b at $z = 0.193$. Note the very steep exponential disk in both *V* and *I*. The galaxy has a bar and two companions with unknown redshift. The positive *Y*-axis of the gray-scale image points to the right. (*f*) As in Fig. 2*a*, but for the field disk galaxy 53W044b with $z = 0.199$. The object was in the corner of an *I*-band CCD, resulting in some inconsistency between Lucy and MR-CLEAN, since the nearest PSF was 200 pixels away (worst case example). Note the rather clumpy and irregular morphology and the very flat exponential disk. The positive *Y*-axis of the gray-scale image points to the right.

ticity shows the usual increase from $e \simeq 0$ in the bulge to $e \simeq 0.5$ where the disk starts to dominate. The ellipticity drops to $e \simeq 0.3$–0.35 where the bar stops. We classify 53W044a as a barred field spiral at $z = 0.131$. The faint barlike structure affects the disk fit (such that the smooth underlying disk has a longer scale length than the global fit would indicate).

6.2. *Field Galaxy 53W002c at z = 0.273*

Figure 4*b* shows the field galaxy 53W002c at $z = 0.273$. It clearly has a exponential disk in both *V* and *I* for $a \gtrsim 0\farcs8$, and an inner $a^{1/4}$-like bulge for $a^{1/4} \lesssim 1.7$ pixels$^{1/4}$, both without major color gradients. The sky position angle shows some peculiar isophotal twist in the inner part of the *V* image, possibly due to an unknown remaining hot pixel. The ellipticity shows the usual increase from $e \simeq 0$ in the bulge to $e \sim 0.25$ where the disk takes off. At very high contrast, the MR-CLEAN image shows no clear spiral arms, but possibly a bar. 53W002c is classified as a field disk galaxy at $z = 0.273$.

6.3. *Field Galaxy 53W002d at z = 0.275*

Figure 4*c* shows the field galaxy 53W002d at $z = 0.275$. It clearly has an exponential disk in both *V* and *I* for $a \gtrsim 1\farcs0$ and a somewhat larger inner $a^{1/4}$-like bulge for $a^{1/4} \gtrsim 1.8$ pixels$^{1/4}$, both without color gradients. The sky position angle shows no isophotal twist, and the ellipticity shows the usual increase from $e \simeq 0$ in the bulge to $e \sim 0.45$ where the disk takes off. At very high contrast, the MR-CLEAN image shows no clear spiral arms, but possibly a bar. 53W002d is classified as a field disk galaxy at $z = 0.275$. The light profiles run into two faint neighboring galaxies (with unknown redshift) for $a \gtrsim 5\farcs0$ (shown to the left in Fig. 4*b*). The dashed line (barely visible in the upper right panel) indicates a MR-CLEAN that was deliberately done with a PSF that had a few saturated central pixels. It is encouragingly similar to the one done with a good PSF (*solid line*), except in the very core of the *V*-band image, where the saturated PSF leads to an ~ 0.2 mag overestimate of the galaxy's core flux.

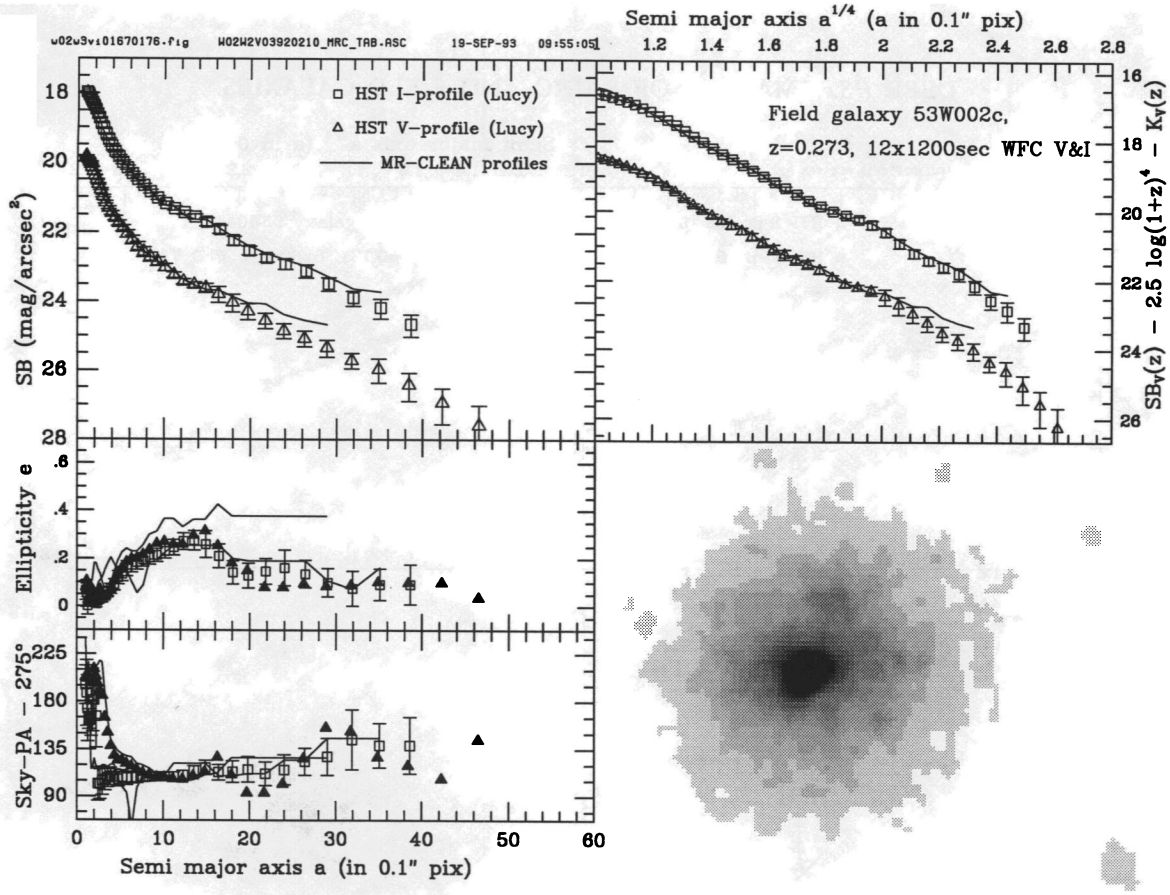

FIG. 4*b*

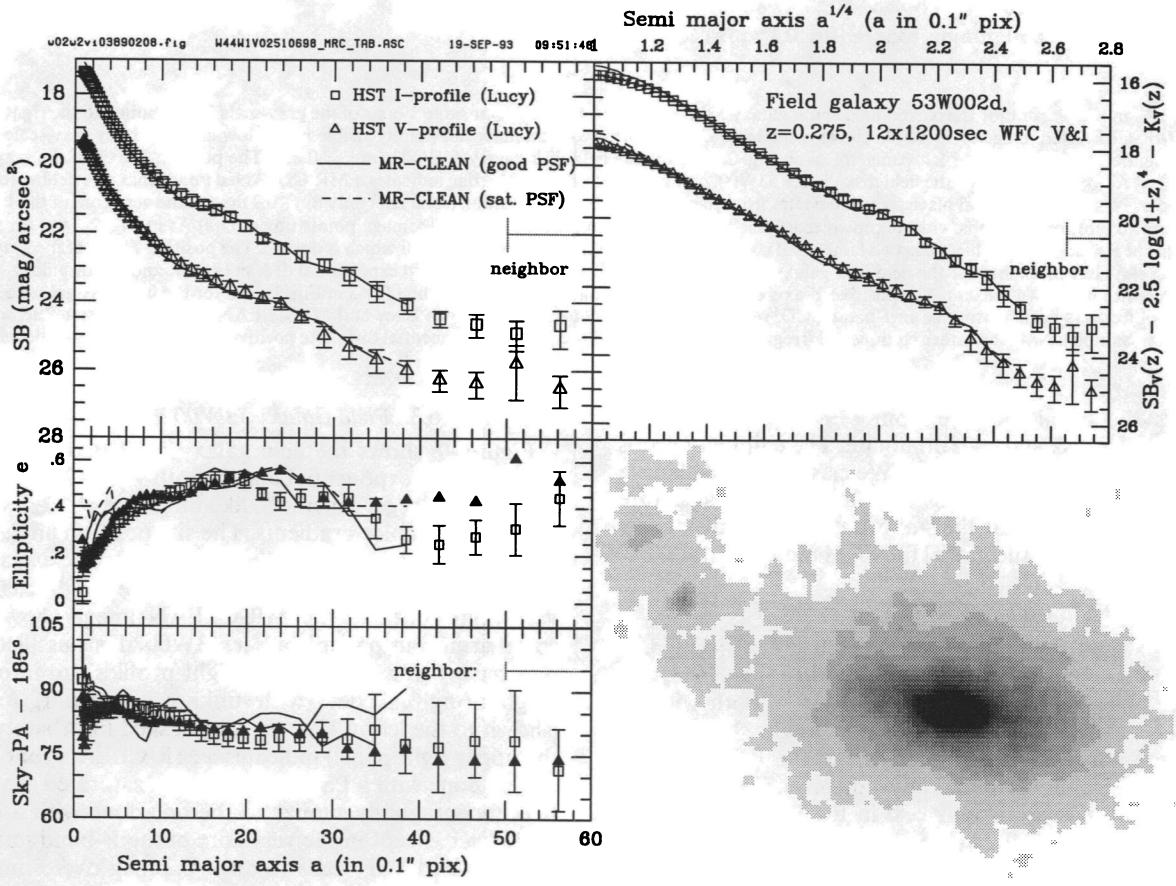

FIG. 4*c*

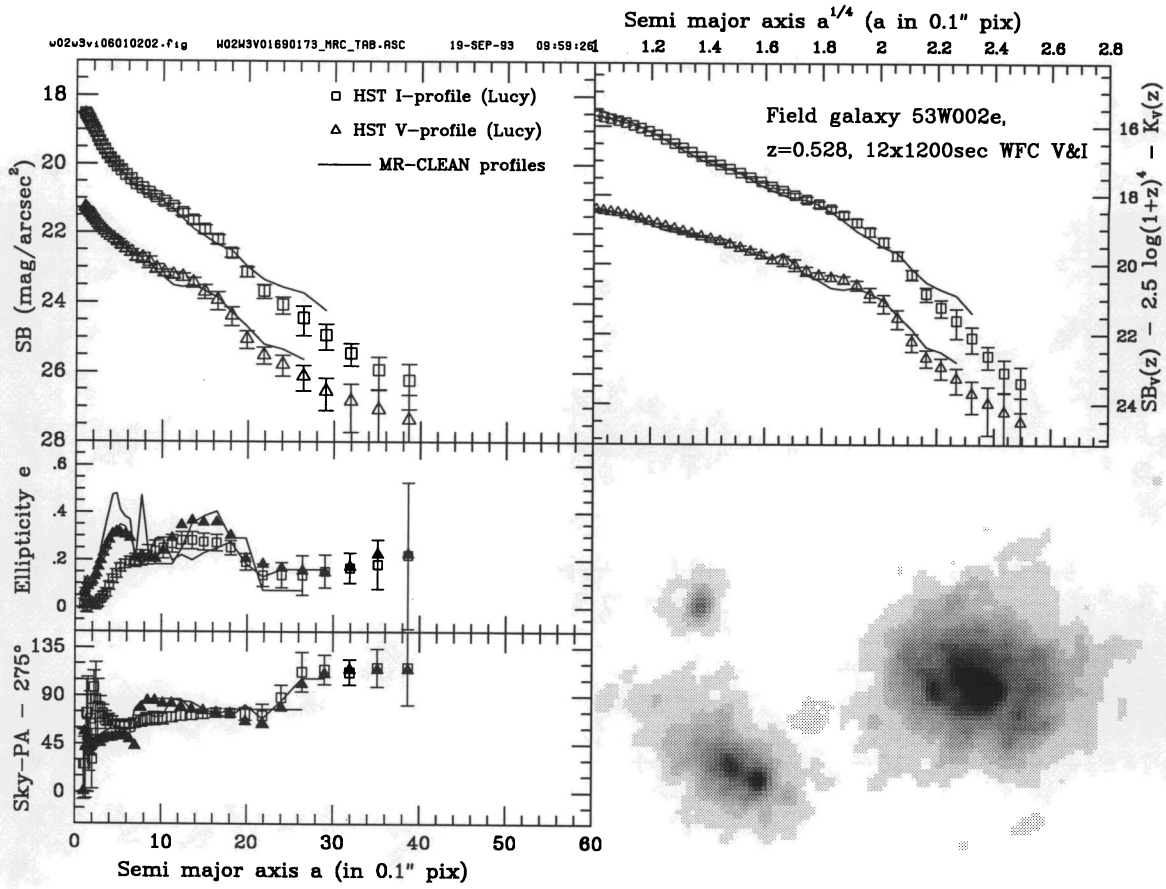

FIG. 4*d*

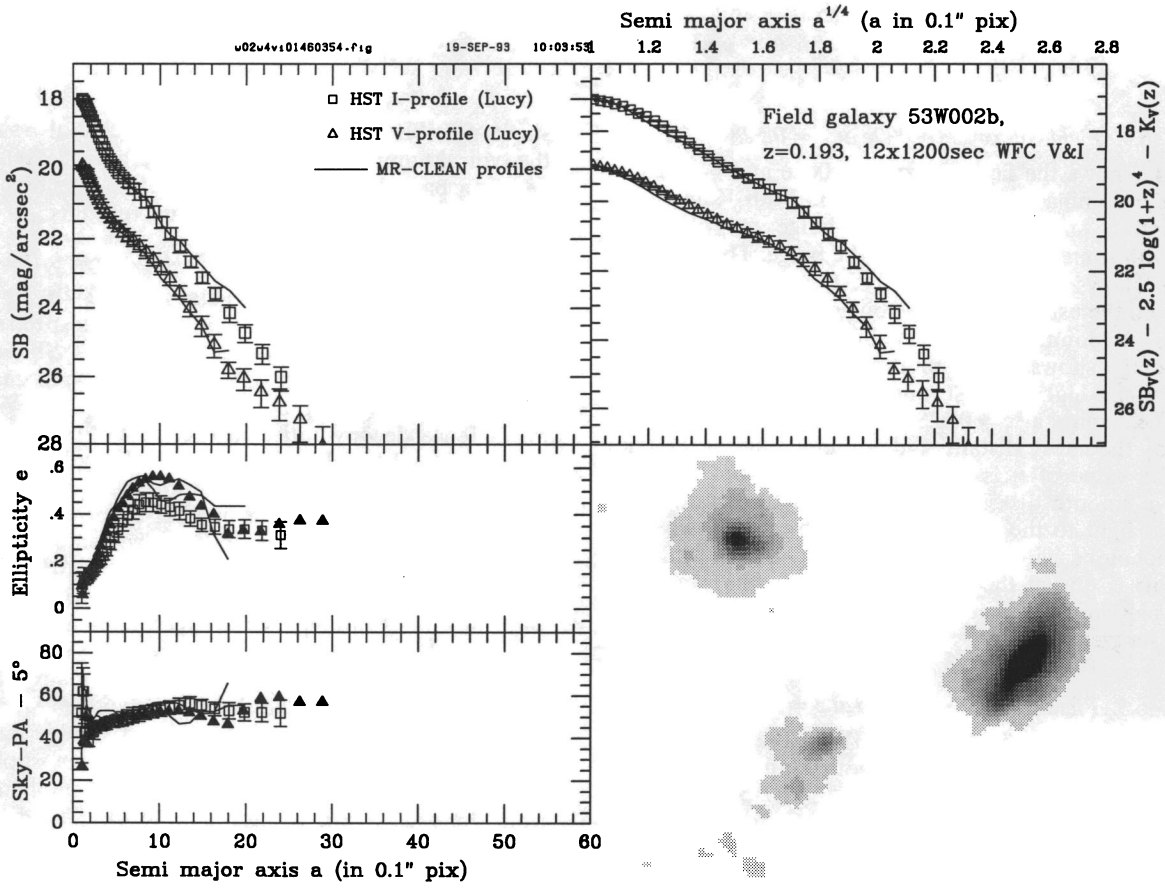

FIG. 4*e*

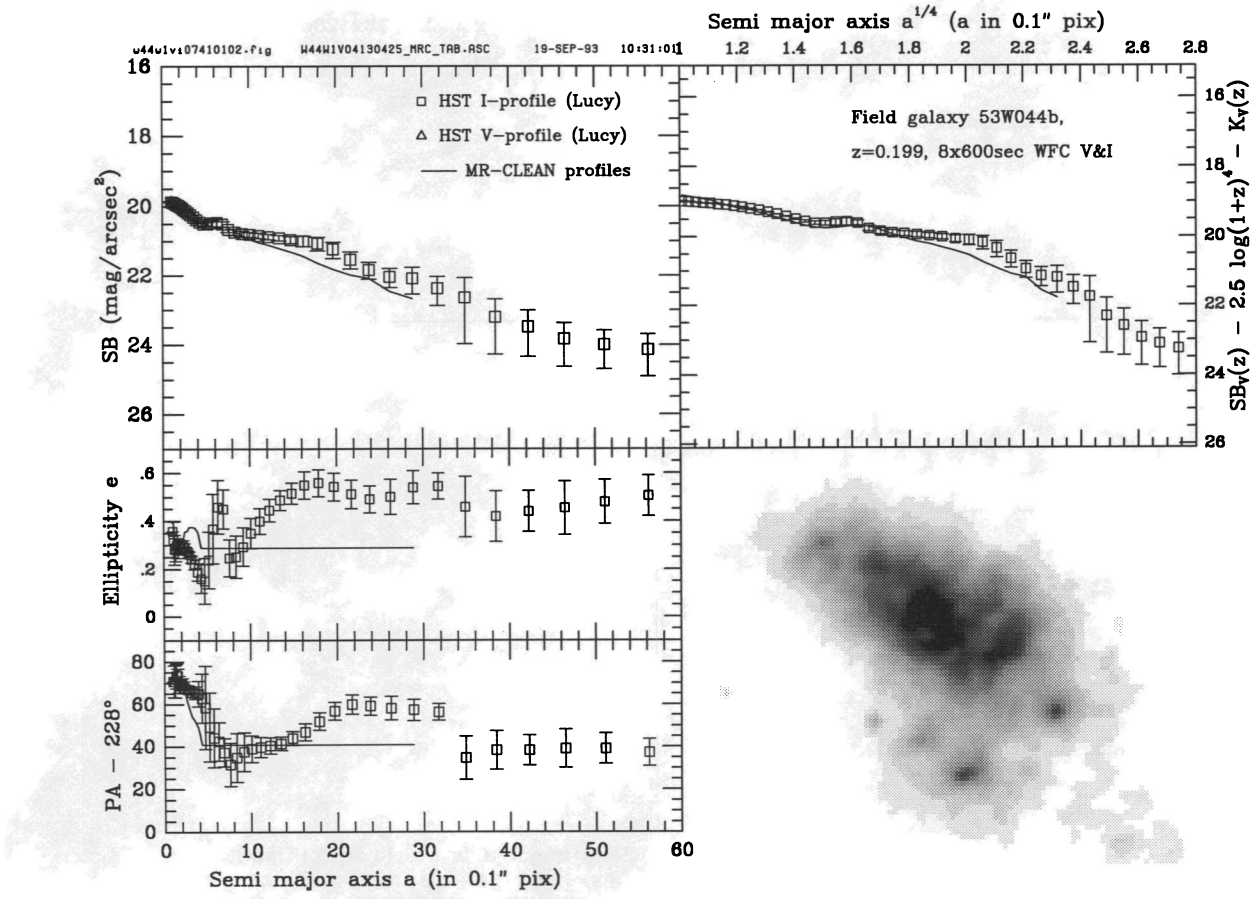

FIG. 4*f*

6.4. *Field Galaxy 53W002e at z = 0.528*

Figure 4*d* shows the field galaxy 53W002e at $z = 0.528$. It clearly has a dominant exponential disk in both V and I for $a \gtrsim 0\farcs6$ and a small inner $a^{1/4}$-like bulge for $a^{1/4} \lesssim 1.8$ pixels$^{1/4}$, with some color gradient in the bulge. The sky position angle shows little isophotal twist, and the ellipticity increase from the usual $e \simeq 0$ in the bulge to $e \sim 0.3$ where the disk starts to dominate. At very high contrast, the MR-CLEAN image shows some spiral structure, only visible in Figure 4*d* after a high-contrast reproduction. 53W002e is classified as a field spiral at $z = 0.528$. At $V = 20.6$ mag, it is possibly one of the most distant and luminous spiral galaxies known. The value of r_s is likely to be underestimated with respect to a smooth disk, as the spiral structure contributes some excess light to the inner disk. The object has two faint small companions with unknown redshift, one of which is double. This is one of the brighter objects in the sample of candidate pairs of Burkey et al. (1994), who discuss the epoch-dependent merger rate.

6.5. *Field Galaxy 53W002b at z = 0.193*

Figure 4*e* shows the field galaxy 53W002b at $z = 0.193$. It has an very steep exponential disk in both V and I for $a \gtrsim 0\farcs6$, and a small inner $a^{1/4}$-like bulge for $a^{1/4} \lesssim 1.7$ pixels$^{1/4}$, with little or no color gradients. The sky position angle shows no isophotal twist, and the ellipticity shows a very steep increase from $e \simeq 0$ in the bulge to $e \sim 0.5$ where the disk starts to dominate. At very high contrast, the MR-CLEAN image shows possibly a bar, the presence of which is also suggested by the typical hump in the e versus a diagram. 53W002b is classified as a barred field spiral at $z = 0.193$. The object has two other faint companions with unknown redshifts.

6.6. *Field Galaxy 53W044b at z = 0.199*

Figure 4*f* shows the field galaxy 53W044b. Its redshift is $z = 0.199$ from weak H and K in the MMT spectrum, consistent with its ground-based colors and its SB. The galaxy appears in a corner of the 53W044 WF1 I-band images, but is intersected by two chip borders of the WF1 and WF2 images in V. Hence, deconvolution in V could not be done, and some inconsistency is produced between the Lucy and MR-CLEAN methods in the I band, since the nearest PSF star was 200 pixels away (fatal for objects in a WFC corner). The modeling was done with a TinyTIM PSF at the same position as the object, but has limited dynamic range, because the galaxy is close to the chip corner. This object is our worst case example with the largest discrepancy between Lucy and MR-CLEAN. Yet, the two methods only disagree by $\lesssim 0.5$ mag arcsec^{-2} in a limited range of a. The object has a rather clumpy and irregular morphology, a very flat dominant exponential disk in I for $a \gtrsim 0\farcs4$, and a very small inner $a^{1/4}$-like bulge for $a^{1/4} \lesssim 1.4$ pixels$^{1/4}$. The sky position angle shows some isophotal twist, that may be due to the PSF mismatch. The ellipticity increases from the usual $e \simeq 0$ in the bulge to $e \sim 0.5$ where the disk starts to dominate. 53W044b is classified as an irregular field galaxy. The object has a faint extension to the bottom, possibly an infalling companion.

7. CONCLUSIONS

The analysis of our *HST* images shows that meaningful surface photometry can be done on field and radio galaxies out to $z \simeq 0.6$ with deconvolved *HST* images down to $\lesssim 0''.2$ FWHM resolution, provided that the objects have sufficient S/N and one uses (nearly) photon-preserving deconvolution routines like the Lucy or MR-CLEAN algorithm. Our main findings are:

1. 53W046 is an ordinary giant elliptical radio galaxy with an $a^{1/4}$-like light profile at $z = 0.528$.

2. 53W044 is an early-type radio galaxy with a dominant $a^{1/4}$ light profile in $V+I$, plus a weak exponential disk. It is likely an S0 at $z = 0.311$. Another field elliptical with $a^{1/4}$ profile was found at $z = 0.58$.

3. 53W002 already has a well-behaved, $a^{1/4}$-like light profile at $z = 2.390$, consistent with that seen in nearby luminous early-type galaxies. At $z = 2.390$, this one radio galaxy is already dynamically relaxed, hence a few crossing times old. The color of 53W002 is $V-I \simeq 0.3 \pm 0.2$ mag in the inner part ($a \sim 0''.2$, affected by its weak AGN) and may grow from $V-I \simeq 1.2 \pm 0.3$ mag at $a \gtrsim 0''.4$ to possibly $V-I \gtrsim 2.2 \pm 0.3$ mag at $a \gtrsim 1''.2$. Together with its rather constant $I-K$ color ($\simeq 2.5$ mag for $a \gtrsim 1''.0$–$1''.5$), this is consistent with an aging stellar population that is ~ 0.3–0.5 Gyr old in the galaxy center ($a \lesssim 2$ kpc radius) and possibly ~ 0.5–1.0 Gyr at $a \gtrsim 10$ kpc radius. Within the errors, its dynamical age is consistent with that of the stellar population, so that its dynamical collapse and its first major burst of star formation likely started at about the same time, or ~ 0.5–1 Gyr before $z = 2.390$ in its outskirts and $\lesssim 0.3$–0.5 Gyr in its center, the latter possibly still boosted by the jet. Our *HST* images of 53W002 suggest that stars in spheroidal components were formed rather quickly and possibly as late as $z_{\rm form} \lesssim 2.5$–$4$ (for $H_0 = 50$ and $q_0 = 0.1$), on a timescale comparable to the collapse time of the protogalaxy ($\lesssim 1$ Gyr), consistent with the classical galaxy halo collapse model of Eggen et al. (1962).

4. Six field galaxies with redshifts $z = 0.131$–0.528 have typically dominant exponential disks in both V and I ($a \gtrsim 0''.4$–$1''.0$) and (small) inner $a^{1/4}$-like bulges for $a^{1/4} \lesssim 1.4$–1.8 pixels$^{1/4}$, with little or no color gradients. The sky position angle usually shows little or no isophotal twist (except in the cases of bars), and the ellipticity increases from the usual $e \simeq 0$ in the bulge to $e \simeq 0.3$–0.5 where the disk starts to dominate (plus a significant drop from the bulge out into the disk in case of bars). At very high contrast, the MR-CLEAN image sometimes shows spiral structure or a bar. About half of the galaxies have faint companions, and one has irregular structure.

5. We bootstrapped the unknown FOC/48 zero point to $m_{2750} = 21.34 \pm 0.09$ mag (for 1.00 counts s^{-1}) using three independent measurements. FOC/48 2750 Å fluxes were detected for both 53W044 and 53W046. Because their redshifts are 0.311–0.528, the 2750 Å filter samples these galaxies around 1800–2100 Å in the rest frame, where the SEDs of nearby early-type galaxies go through a minimum. Their FOC/48 fluxes will be discussed together with Cycle 2 FOS spectra in separate papers to constrain the evolution of the UV upturn in early-type galaxies (W94b; Pascarelle et al. 1994).

We thank R. Lucas, B. Gillespie, D. Golombek, and the STScI staff for their continuous help in this project; C. Heller, J. Robertson, J. McAffee, and D. Means for assistance at the MMT and Steward 90 inch telescopes; D. Mathis, A. Ferro, and A. Willis for help in taking the MMT spectra and 90 inch images; P. Katgert for help in retrieving some radio maps; D. Burstein, J. Hester, and T. Lauer for useful discussions; and the referee for useful suggestions that helped improve our presentation.

We thank the directors of the MMT and Steward Observatory for the generous allocation of telescope time. The United Kingdom Infrared Telescope is operated by the Joint Astronomy Centre, Hilo, on behalf of the Royal Observatory, Edinburgh. This work was supported by NASA Cycle 1 grant GO-2405.01-87A (to both R. A. W. and W. C. K.) from STScI, which is operated by AURA, Inc., under NASA contract NAS5-26555. Ground-based follow-up work was also supported by NSF grant AST-8821016 and the Alfred P. Sloan Foundation (to R. A. W.).

REFERENCES

Bertola, F., Bressan, A., Burstein, D., Buson, L. M., Chiosi, C., & Di Serego Alighieri, S. 1993, in Science with the *Hubble Space Telescope*, ed. P. Benvenuti & E. Schreier (ESO Conf. Proc. 44) (Munich: ESO), 143
Bruzual A., G. 1981, Ph.D. thesis, Univ. California
———. 1983, ApJ, 273, 105
———. 1988, in Towards Understanding Galaxies at Large Redshift, ed. R. G. Kron & A. Renzini (Dordrecht: Kluwer), 161
Burkey, J. M., Keel, W. C., Windhorst, R. A., & Franklin, B. E. 1994, ApJ, 429, 13
Burstein, D., & Heiles, C. 1982, AJ, 87, 1165
Chambers, K. C., Miley, G. K., & van Breugel, W. J. M. 1990, ApJ, 363, 21
de Vaucouleurs, G., de Vaucouleurs, A., & Corwin, H. 1976, Second Reference Catalog of Bright Galaxies (Austin: Univ. Texas Press)
Dressler, A., Oemler, A., Butcher, H., & Gunn, J. E. 1994, ApJ, 430, 107
Dressler, A., Oemler, A., Gunn, J. E., & Butcher, H. 1993, ApJ, 404, L45
Dunlop, J. S., & Peacock, J. A. 1993, MNRAS 263, 936
Eales, S. A., & Rawlings, S. 1993, ApJ, 411, 67
Eggen, O. J., Lynden-Bell, D., & Sandage, A. 1962, ApJ, 136, 748
Griffiths, R. G. 1990, in *HST* Wide Field and Planetary Camera Instrument Handbook, Ver. 2.1 (Baltimore: STScI; see also ver. 3.0, 1992) (G90)
Griffiths, R. E., et al. 1993a, in the Milano Int. Symp. Observational Cosmology, ed. G. Chincarini, A. Iovino, T. Maccacaro, & D. Maccagni (ASP Conf. Ser., 51), 320
———. 1993b, in Science with the *Hubble Space Telescope*, ed. P. Benvenuti & E. Schreier (ESO Conf. Proc. 44) (Munich: ESO), 13
———. 1994, ApJ, in press (G94)
Harris, H. C., Baum, W. A., Hunter, D. A., & Kreidl, T. J. 1991, AJ, 101, 677
Hasan, H., & Burrows, C. J. 1993, STScI Image Restoration Newsletter, 1, 54
Heckman, T. M., Miley, G. K., Balick, B., van Breugel, W. J. M., & Butcher, H. R. 1982, ApJ, 262, 529
Hogbom, J. A. 1974, A&AS, 15, 417
Holtzman, J. A., et al. 1991, ApJ, 369, L35
Hunter, D., Faber, S., Light, R., & Shaya, E. 1992, in Final Orbital/Science Verification Report of the WF/PC IDT, ed. S. M. Faber & J. A. Westphal (Baltimore: STScI), 1
Jacoby, G. H., Hunter, D. A., & Christian, C. A. 1984, ApJS, 56, 257
Keel, W. C. 1991, PASP, 103, 723
Keel, W. C., & Windhorst, R. A. 1991, ApJ, 383, 135
———. 1993, AJ, 106, 455 (KW93)
King, I. R., Stanford, S. A., Seitzer, P., Bershady, M. A., Keel, W. C., Koo, D. C., Weir, N., Djorgovski, S., & Windhorst, R. A. 1991, AJ, 102, 1553 (K91)
Kristian, J. A. 1973, ApJ, 179, L61
Kron, R. G., Koo, D. C., & Windhorst, R. A. 1985, A&A, 146, 38 (KKW)
Lauer, T. 1989, PASP, 101, 445 (L89)
Lucy, L. B. 1974, AJ, 79, 745
McCarthy, P. J., Kapahi, V. K., & van Breugel, W. J. M. 1990, ApJ, 365, 487
McCarthy, P. J., Spinrad, H., Djorgovski, S. G., Strauss, M. A., van Breugel, W. J. M., & Liebert, J. 1987, ApJ, 319, L39
McClure, R. D., Pierce, M. J., & Lavery, R. J. 1993, BAAS, 25, 838
McLean, I. S., Chuter, T. C., McCaughrean, M. J., & Rayner, J. T. 1986, Proc. SPIE, 627, 430
Miley, G. K., Chambers, K. C., van Breugel, W. J. M., & Macchetto, F. 1992 ApJ, 401, L69
Mutz, S. B., Windhorst, R. A., Pascarelle, S. M., Schmidtke, P. C., Griffiths, R. E., Ratnatunga, K. U., Casertano, S., & Im, M. 1994, ApJ, 434, L55
O'Connell, R. W. 1993, private communication

Oke, J. B., & Gunn, J. E. 1983, ApJ, 266, 713
Oort, M. J. A. 1987, Ph.D. thesis, Univ. Leiden
Oort, M. J. A., Katgert, P., Steeman, F. W. M., & Windhorst, R. A. 1987, A&A, 179, 41
Paresce, F. 1990, *HST* Faint Object Camera Instrument Handbook, ver. 2.0 (Baltimore: STScI)
———. 1992, *HST* Faint Object Camera Instrument Handbook, ver. 3.0 (Baltimore: STScI)
Pascarelle, S. M., Windhorst, R. A., Keel, W. C., Bertola, F., McCarthy, P. J., O'Connell, R. W., Renzini, A., & Spinrad, H. 1994, AJ, in preparation
Ratnatunga, K. U., et al. 1994, AJ, 108, in press
Seaton, M. J. 1979, MNRAS, 187, 73
Smith, E. P., et al. 1992 ApJ, 295, L54
Sparks, W. B. 1992, in Faint Object Camera Science Verification Report, ed. P. Greenfield et al. (Baltimore: STScI), FOC-053
Thuan, T. X., Windhorst, R. A., Puschell, J. J., Isaacman, R. B., & Owen, F. N. 1984, ApJ, 285, 515
Van Albada, T. S. 1982, MNRAS, 201, 939
Wakker, B. P., & Schwartz, U. J. 1988, A&A, 200, 312 (WS)
White, R. L. 1993, STScI Image Restoration Newsletter, 1, 11
Windhorst, R. A., Ferro, A. J., Gordon, J. M., Mathis, D. F., Neuschaefer, L. W., & Keel, W. C. 1993a, in Science with the *Hubble Space Telescope*, ed. P. Benvenuti & E. Schreier (ESO Conf. Proc. 44) (Munich: ESO), 21 (W93a)
Windhorst, R. A., Fomalont, E. B., Partridge, R. B., & Lowenthal, J. D. 1993b, ApJ, 405, 498 (W93b)
Windhorst, R. A., Franklin, B. E., & Neuschaefer, L. W. 1994a, PASP, 106, 798 (W94a)
Windhorst, R. A., Koo, D. C., & Spinrad, H. 1986, in Galaxy Distances and Deviations from Universal Expansion, ed. B. F. Madore & R. B. Tully (Dordrecht: Reidel), 197
Windhorst, R. A., Kron, R. G., & Koo, D. C. 1984a, A&AS, 58, 39 (WKK)
Windhorst, R. A., Mathis, D. F., & Keel, W. C. 1992, ApJ, 400, L1 (W92)
Windhorst, R. A., Mathis, D. F., Neuschaefer, L. W. 1990, in Evolution of the Universe of Galaxies (Edwin Hubble Centennial Symposium), ed. R. G. Kron (ASP Conf. Ser., 10), 389 (W90)
Windhorst, R. A., Miley, G. K., Owen, F. N., Kron, R. G., & Koo, D. C. 1985, ApJ, 289, 494
Windhorst, R. A., Pascarelle, S. M., Keel, W. C., Bertola, F., McCarthy, P. J., O'Connell, R. W., Renzini, A., & Spinrad, H. 1994b, in Frontiers of Space and Ground-based Astronomy, Vol. 187, ed. W. Wamsteker, M. S. Longair, & Y. Kondo (Dordrecht: Kluwer), 663 (W94b)
Windhorst, R. A., van Heerde, G. M., & Katgert, P. 1984b, A&AS, 58, 1 (WHK)
Windhorst, R. A., et al. 1991, ApJ, 380, 362 (W91)
———. 1994c, AJ, 107, 930 (W94c)
Wu, C.-C., et al. 1991, NASA *IUE* Newsletter, 43, 1